Results in Engineering 30 (2026) 109713

Contents lists available at ScienceDirect

Results in Engineering

journal homepage: www.sciencedirect.com/journal/results-in-engineering

Research paper

A compact super wideband 5 G Hilbert slot antenna for wearable and IoT applications

Sarmad Nozad Mahmood [a], Sahar Saleh [b,c], Ahmed Nidham Qasim [a], Tale Saeidi [b,d]

[a] Medical Instrumentation Techniques Engineering Department, Technical Engineering College – Kirkuk, Northern Technical University, Mosul 41001, Iraq
[b] WiSAR Lab, Atlantic Technological University (ATU), Letterkenny, Co. Donegal F92 YY97, Ireland
[c] Department of Electronics and Communications Engineering, Faculty of Engineering, University of Aden, Aden 5243, Yemen
[d] Electrical and Electronics Engineering Department, Faculty of Engineering and Natural Sciences, Istinye University, Istanbul 34326, Turkey

ARTICLE INFO

Keywords:
Hilbert slot antenna (HSA)
Wideband antenna
5 G mmWave antenna
Wearable antenna
Super wideband (SWB)
Frequency range 2 (FR2)
Specific absorption rate (SAR)
Wearable body area network (WBAN)
CST

ABSTRACT

This work presents the design, fabrication, and measurement of a compact, super-wideband (SWB) 5 G mmWave Hilbert Slot Antenna (HSA) that includes all Frequency Range 2 (FR2) bands (n257-n263). The antenna is fabricated on a semi-flexible Rogers RT/Duroid 5880 substrate, known for its low losses at high frequencies ($\mathcal{E}_r = 2.2$, $h = 0.508$ mm, $\tan(\sigma) = 0.004$). Despite its small size of 7.31 × 7.31 mm^2, the proposed antenna achieves an impressive measured super-wide bandwidth of 39.1 GHz, with a peak gain of 7.22 dBi. The design evolution of the HSA is thoroughly explored, focusing on the effects of iteration, segment count, and feed point location on antenna performance. Parametric studies reveal the antenna's optimized configuration, showcasing significant bandwidth improvements and a reduced size compared to other designs. The antenna's suitability for wearable, body-centric applications is discussed, with an emphasis on mechanical modifications and its performance near the human body. Additionally, the Specific Absorption Rate (SAR) values are evaluated and found to be within the safety limits, ensuring the antenna's compliance with electromagnetic radiation exposure standards. The proposed antenna design has a wide bandwidth, compact size, and optimal performance, outperforming other fractal designs with a simpler geometry and fewer iterations, making it an excellent candidate for 5 G communication systems and wearable devices.

1. Introduction

Wearable intelligent systems in Wireless Body Area Networks (WBAN) are rapidly evolving, with applications spanning healthcare, entertainment, surveillance, and safety. These systems are often integrated into clothing and require strong connectivity for off-body use and precise detection for on-body applications to mitigate reflections from lossy body tissues. Recent advancements in millimeter-wave communication systems have driven the need for compact, high-performance antennas capable of operating in the super-wideband (SWB) frequency range (all the FR2). These frequencies are ideal for next-generation wireless communication, particularly in wearable and body-centric applications where low cost, size, and efficient performance in terms of high gain and high data rate are essential [1]. SWB enables deep penetration at lower frequencies (e.g., aiding in tumor detection) and high-resolution precision at higher frequencies with a wide bandwidth [2–4].

Antennas are essential for wearable applications, serving as a crucial component that connects wearable devices to wireless network nodes. Wearable antennas must be designed to offer a wide bandwidth (BW), high gain, compact size, flexibility, and durability to withstand mechanical changes [3]. Due to the unique advantages of Hilbert slot antennas (HSA), including compact size, wide BW, high gain, and efficient integration capabilities, they serve as excellent candidates for mmWave 5 G wearable applications [5]. The fractal structure of Hilbert antennas (HAs) enables significant miniaturization while maintaining high performance across wide frequency ranges, making them ideal for both off-body communication (e.g., enhancing connectivity in wireless networks) and on-body applications (e.g., improving the accuracy of microwave imaging systems). Additionally, their design supports flexibility and robust operation under mechanical deformation, a critical requirement for wearable systems. These characteristics position HSAs as a superior alternative to traditional antenna designs for WBAN applications.

The work in [6] presented a compact, semi-flexible, dual-band wearable antenna (1.38–1.8 GHz and 2.25–4.88 GHz) based on Moore's fractal geometry derived from the Hilbert curve. This design offered low SAR characteristics and was specifically targeted for use in biotelemetry applications within biomedical diagnostic systems. To suppress surface wave coupling, a Hilbert fractal band-stop filter based on composite right/left-handed (CRLH) metamaterial (MTM) was incorporated into a compact multi-band (2–3 GHz, 3.4–3.9 GHz, 4.4–5.2 GHz) 4-element

https://doi.org/10.1016/j.rineng.2026.109713
Received 10 August 2025; Received in revised form 6 January 2026; Accepted 22 February 2026

MIMO antenna array utilizing Sierpiński fractal radiators proposed for 5 G communication systems [7]. BW and near-field isolation were further improved by using a staircase-shaped ground structure with alternating low, high, and low impedance sections. A compact wideband (0.367–3 GHz) conformal capsule antenna based on Hilbert fractal geometry was designed in [8] for a miniaturized biomedical telemetry system. In [9], a compact fourth-order HA for 100–300 MHz RF energy harvesting was proposed, featuring a cross-finger structure with six intersecting arms to enable miniaturization via equivalent capacitance and inductance. Paired with a Schottky-based voltage-doubling rectifier, the design achieved an efficiency of 78%, demonstrating strong potential for low-frequency energy collection. A hybrid circularly polarized (CP) fractal antenna combining 2nd-order Vicsek-cross and Koch (VKFA) curves was proposed for Ku-band applications, which improves miniaturization, BW (16.92 to 18.74 GHz), making it suitable for satellite and radar systems [10]. The CP is achieved via two orthogonal L-shaped slots in its radiator. In a recent study [11] a compact, wideband (5.82–9.55 GHz) semi-flexible Hilbert curve-based antenna (HCA) was introduced for WBAN applications, covering WiFi 6E, upper C-band, and lower X-band frequencies. Performance assessments using both flat and voxel human phantoms demonstrated stable radiation characteristics and low Specific Absorption Rate (SAR) values, confirming the antenna's mechanical resilience and suitability for wearable use.

At mmWave frequencies, achieving high gain and radiation efficiency is challenging due to signal blockage, material losses, and increased path loss from the short wavelength. Various strategies have been proposed to address these issues. The following paragraphs provide an overview of general fractal geometries, followed by a focus on well-known types, including Sierpinski, Minkowski, Hilbert, and Koch.

A tree-shaped fractal (26–30.2 GHz) antenna was designed for future 5 G communication, utilizing a finite rectangular ground and optimized substrate dimensions [12]. A compact 1 × 4 planar fractal array antenna for 5 G mmWave [13] achieves wide BW (22.8–29.2 GHz), high gain (10.7 dBi), and greater than 95% efficiency. It uses a 4th-iteration rhombus-inscribed circular fractal radiator, a square-notch partial ground, and a corporate feed network. The authors in [14] presented a fractal antenna with an integrated substrate gap waveguide (ISGW) for 5 G mm-wave communication, achieving wide BW (24.72–40.20 GHz) and 9 dB gain, offering a compact and efficient design for modern applications. However, a vertical cascade T-shaped fractal-like antenna is proposed in [15] for V-band 5 G applications, offering wideband performance (59–68 GHz) with an average gain of over 6.5 dBi. The data-driven evolutionary algorithm using a selective ensemble (DDEA-SE) is employed in [16] to optimize the design of the proposed fractal arrow-shaped mmWave multi-band (15.9–17.2 GHz, 22.9–25.9 GHz, and 27.64–28.48 GHz) flexible wearable antenna for IoT and 5 G Communication Systems. An Artificial Neural Network (ANN) is employed in [17] to optimize the 16% reduction in size of a compact wideband (27–33 GHz) microstrip patch antenna with an H-shaped fractal defected ground structure (DGS), designed for vehicular communication applications. A compact 4-port orthogonally placed cross-fractal MIMO antenna with wide BW (15.97–45.12 GHz) and high isolation is presented in Enahoro et al. (2023), using coplanar waveguide (CPW) feeding and a 3 × 3 array of double square split ring (DSSR) metamaterial resonators in the ground, making it well-suited for 5 G K, Ka, and mmWave applications [18]. A novel fractal antenna based on a circular geometry was designed in [19] using iterative shape removal to achieve multi-band performance at 24.64, 35.65, and 42 GHz, which is suitable for 5 G mmWave applications.

L-shaped (26.76–29.43 GHz) array [20] and compact broadband (25–27 GHz and 27.5–37.9 GHz) slot antenna [21] are proposed for 5 G cellular communication and 5 G femtocell systems applications, utilizing first- and second-order fractal Sierpinski gaskets, respectively. At the same time, a wide BW (58.3–61.7 GHz) patch antenna is proposed in [22] for WBAN applications using a Minkowski–Sierpinski fractal geometry with a substrate-integrated waveguide (SIW). Designed for 5G-enabled mobile devices and machine-to-machine communication, the antenna incorporates composite CRLH structures to minimize inter-element coupling. In [23], the performance (BW, gain, and radiation) of the proposed mmWave 5 G Sierpinski carpet fractal multi band (29.5–32.6 & 37.5–38.5) patch antenna is enhanced by etching Sierpinski gasket and carpet structure slots in the ground, integrated with DGS and SIW techniques, making it suitable for mmWave 5 G and ground-based radio navigation applications. A modified Sierpinski Carpet fractal shape and quadrant circular ring fractal DGS are used in [5] to improve the BW of the proposed multi-band (28.4–38.5 GHz, 24.7–25.7 GHz, 32.6–36.5 GHz, and 37.5–38.6 GHz) patch antenna for ground-based radio navigation applications. A compact, reconfigurable HA with a PDLC substrate enables discrete and continuous frequency tuning from 0.2 to 0.6 THz, achieving a shift of up to 17% and a gain of 8.43 dBi [24]. Its tunability, small size, and high directivity make it suitable for secure satellite, military, and portable communication systems.

Mondir et al. (2023) proposed a compact 1 × 3 patch antenna array operating at 27–30.86 GHz for mmWave 5 G applications, where wide bandwidth and miniaturization were achieved by integrating a complementary infinite split ring resonator (CI-SRR) on the radiator and a Hilbert fractal on the ground plane [25]. To enhance isolation and minimize mutual coupling, CRLH structures were incorporated on the antenna's backside. A hybrid fractal MIMO antenna combining Minkowski and Koch curves on a half-octagonal patch was proposed for wideband 5 G (23.9–30 GHz) and UWB (1–21.4 GHz) applications [26]. The wide BW and high isolation are achieved using a tapered feed and a modified ground. A modified fractal antenna based on multiple rectangular slots is proposed in [27] suitable for 5 G mmWave applications. In [28], a multi-band (17–28 GHz, X-band (8.9–9.9 GHz, 10.4–11.4 GHz), and Ku-band (13.1–13.7 GHz, 15.4–16.2 GHz)) MIMO patch antenna with a 3rd iteration spherical-shaped fractal slot is designed for 5 G mm-wave applications. However, the enhancement of the proposed wideband (26.5–40 GHz) Koch-shaped path antenna in [29] is achieved through the integration of Koch curves with a DGS, making it highly suitable for telemedicine, IoT, and 5 G millimeter-wave applications. A 2 × 2 MIMO multi-band antenna operating at 25.52–28.23 GHz, 36.5–37.5 GHz, and 47.7–49.7 GHz was developed for 5 G and IoT mobile terminals using a second-order Minkowski fractal design [30].

Table 1 provides a comprehensive summary of the various wearable fractal antennas that have been proposed in the literature, highlighting their advantages and disadvantages with regard to performance, applications, and compactness. The Table discusses different fractal shape antennas for a wide range of operational frequencies starting from low 5 G frequency bands, [6–11] to mmWave bands [12,19,26–32]. Although at 5 G low frequency other than mmWave, the size tends to be large, the designs in [6–11] are small, and this is due to the use of the fractal pattern. Even while the designs in [6–8,11] show exciting potential for wearable and medical applications, they nevertheless have a number of drawbacks. In particular in [7,11] do not incorporate actual application analysis, whereas [8] does not incorporate mechanical testing, on-body evaluation, SAR analysis, or experimental validation. Furthermore, the antennas in [9,10] which are not intended for wearable use, have drawbacks like poor gain, lossy substrates, and a limited range of applications.

The mmWave antennas in [5,12–16,19,20,27–29,31,32] are compact owing to their small electrical lengths, achieving smaller sizes compared to others [17,23,26,30]. The fractal geometries help in improving the BW performance, resulting in wide [5,12,13,17,20,23,27,28,32], ultra-wide [14,15,21,29–31], and even super-wide [19] BWs. Despite the 29.2 GHz BW achieved in [19], the proposed SWB HSA surpasses it, providing a broader BW of 39.1 GHz.

Furthermore, as summarized in the comparison table, despite the promising features of existing mmWave antennas, several limitations persist. Many reported designs lack validation through real-world

Table 1
The pros and cons of the state-of-the-art wearable fractal antennas.

Refs.	Type	Dimensions (mm × mm × mm)	Pros	Cons
[6]	Hybrid (Moore & Hilbert)	25.31 × 17.44 × 0.75	-Dual-band (1.38–1.8 GHz & 2.25––4.88 GHz) -Compact & semi-flexible -Low SAR -Suitable for biomedical telemetry	-Lack of mechanical test
[7]	Hybrid (Sierpinski & Hilbert), 4 Ports MIMO	40 × 30 × 1.67 (MIMO) 20 × 30 × 1.67 (Single)	-Multi bands: 2 – 3 GHz, 3.4–3.9 GHz, and 4.4–5.2 GHz -Improved BW (using CPW) and isolation (using CRLH BPF) -Compact	-Lossy FR4 substrate -Lacks proof of real application (e.g., 5 G communication link analysis)
[8]	Hilbert	15 × 39 × 0.508	-Wideband (0.367–3 GHz) -Miniaturized telemetry system -Conformal design	-Lacks an experimental validation -SAR and bending performance not evaluated (wearable use) -Degradable materials not addressed
[9]	Hilbert	274.86 × 144.38 × 2	-Compact -BW improvement using CPW	-Narrow, non-continuous band: 100–300 MHz -Low gain -Non-planar rectifier, not on-board
[11]	Hilbert	11.85 × 14 × 0.508	-Compact -Wideband (5.82–9.55= 4.73 GHz) -Stable SAR on flat & voxel phantoms -Mechanically resilient	-Lacks proof of real application (e.g., WiFi 6E communication link analysis) -Lacks consideration of fully flexible or non-fabric substrates
[10]	Hybrid (Vicsekcross & Koch)	36.6 × 36.6 × 1.6	-Ku-band (16.9–18.7 GHz) -CP radiation -Compact -Moderate gain	-Narrow application scope -Lossy material -Low gain
[12]	Tree-shaped	8 × 13 × 0.6	-Moderate wide BW (26–30.2 = 3.8 GHz =) -Simple design -Moderate gain -Compact	-Lacks an experimental validation
[5]	Sierpinski Carpet patch	15 × 15 × 1.6	-Multi-band (28.4–38.5 = 10.1 GHz, 24.7–25.7 = 1 GHz, 32.6–36.5 = 3.9 GHz & 37.5–38.6 = 1.1 GHz) -Compact	-Lacks proof of real application -Lossy material
[13]	Rhombus-inscribed circular fractal array (1 × 4)	28 × 17.75 × 0.51	-Wideband (22.8–29.2 = 6.4 GHz) • -High gain (10.7 dBi) -Compact	-Lacks proof of real application (5 G communication link analysis)
[14]	electromagnetic dipole fractal antenna with ISGW	NA	-Ultra Wide BW (24.7–40.2 = 15.5 GHz) -high gain -Compact	-Lacks an experimental validation -Complex integration (multilayer ISGW)
[15]	Vertical cascade T-shaped	16 × 18 × 0.79	- Ultra Wide BW (59–68 = 9 GHz) -moderate Gain > 6.5 dBi -Compact	-Lacks an experimental validation
[16]	Arrow-shaped patch	21.81 × 19.5 × NA	Multi-band (15.9 –17.2 = 1.3 GHz, 22.9 –25.9 = 3 GHz & 27.64 – 28.48 = 0.84 GHz) - Moderately low size	-Lacks proof of real application -Lacks an experimental validation for bending -Lacks SAR calculation
[17]	H-shaped	50 × 60 × 1.6	-Wideband (27–33=6 GHz) -ANN-optimized	-Large -Lossy substrate -Lacks proof of real application (e.g., vehicular communication analysis)
[19]	Cross (4-port MIMO) with metamaterials	10.6 × 10.6 × 0.2	-Super wideband (15.9–45.1 = 29.2 GHz) -High isolation -Compact	-Lacks an experimental validation
[21]	Sierpiński gasket	40 × 45 × 0.5	- Ultra Wide BW (25–38=13 GHz) -Good for femtocells	-Not continuous band to 60 -No matching beyond 38 GHz -Large
[27]	Hybrid (Minkowski–Sierpiński) with SIW	6.5 × 9.6 × 0.381	-Wideband (58.3–61.7 = 3.4 GHz) -compact	-Lacks an experimental validation -Complex design considering the via filling
[23]	Sierpiński with DGS + SIW	40 × 40 × 1.6	-Multi-band (24–26.5 = 1.5 GHz, 29.5–36=6.5 GHz) -Improved BW & gain -Suitable for radio navigation.	-Complex ground-plane etching -Not continuous BW as claimed -Lossy substrate -Large
[30]	Hybrid (Minkowski & Koch −2 port MIMO	45 × 75 × 1	-Multi Ultra-wideband (1–21.4 = 19.6 GHz) + 5 G (23.9–30=16.1 GHz) -High isolation	-Large -Lacks proof of real application
[31]	Modified (4-element array)	45 × 75 × 1	- Ultra Wide BW (23.8–34.1 = 10.3 GHz) -Moderately low size	-No far-field measurement is provided -Lacks proof of real application - lossy substrate -The measured S_{11} was not reported very well
[28]	spherical 2-port MIMO	44 × 28.22 × 1.6 (MIMO)	-Multi-band (X-band (8.9–9.9 = 1 GHz, 10.4–11.4 = 1 GHz), and Ku-band (13.1–13.7 = 0.6 GHz, 15.4–16.2 = 0.8 GHz), 17–28=11 GHz)	-Increased complexity -Lossy material -Not continuous BW (X and KU

(*continued on next page*)

Table 1 (*continued*)

Refs.	Type	Dimensions (mm × mm × mm)	Pros	Cons
		28.22 × 28.22 × 1.6 (Single)	-Moderately low size -High isolation -Moderate wide BW	bands) -Lacks proof of real application
[29]	Koch	9 × 9 × 0.8	-Ultra Wideband (26.5–40=13.5 GHz) -Suitable for IoT, telemedicine -compact	-Not continuous BW -Lacks proof of real application
[32]	Minkowski (2 × 2 MIMO)	NA	-Multi-band 25.52 – 28.23=2.71 GHz, 36.5 GHz – 37.5 = 1 GHz, and 47.7 GHz – 49.7 = 2 GHz -Compact	-Lacks an experimental validation -Lacks proof of real application - Not continuous BW
[20]	Sierpiński (L-shaped array)	129.2 × 7.2 × 0.508	-Moderate BW26.7–29.4 = 2.4 GHz -Compact	-Lacks an experimental validation -Lacks proof of real application

applications [5,13,17,20,28–32], SAR calculation [16]or experimental measurements [12,14–16,19,20,27,31,32]. Others exhibit non-continuous BW responses [21,23,28,29], structural complexity [14,23,27,28] or employ lossy substrates [5,17,23,28,31]. In contrast, our proposed fractal antenna demonstrates a broader, continuous BW with a simpler geometry and robust experimental validation, confirming its practical potential for mmWave applications.

Based on the fractal antennas explained in the literature above and the comparison table (Table 1), the HSA is selected in this work for its simple yet effective fractal geometry, enabling compactness and super-wideband operation. Unlike hybrid fractal designs such as Minkowski-Koch or Sierpinski-Hilbert, the HSA requires fewer iterations and segments to achieve similar or better bandwidth, simplifying fabrication while maintaining high gain and robust wearable performance.

In this work, based on the design equations in [31], SWB (24–64 GHz) 5 G mmWave HSA including all the Frequency range (FR2) bands (n257-n263) is designed, fabricated, and measured using a semi flexible Rogers RT/.Duroid 5880 substrate with low losses at high frequencies (ε_r= 2.2 and $h = 0.508$ mm, $\tan\sigma = 0.004$). In addition to this section, Section 2 of this paper covers the simulation process, focusing on design modifications, parametric studies, the effects of body proximity and bending, as well as the calculation of SAR values. Section 3 presents the results and their corresponding discussions, while Section 4 discusses the limitations and future work. Finally, Section 5 provides the concluding remarks of the research. Based on the Finite Integration Technique (FIT), Computer Simulation Technology (CST) is used for the simulations in this work.

2. Simulation

This section explores the design process of the proposed Hilbert slot antenna (HSA), highlighting the iterative design evolution that led to its final optimized configuration. Comprehensive parametric studies are conducted to ensure the antenna achieves optimal parameters for high performance. Section 2.1 focuses on design evolution and parametric analyses. In contrast, Section 2.2 examines the antenna's suitability for wearable, body-centric applications, focusing on mechanical modifications and performance near the human body. Section 2.3, the Specific Absorption Rate (SAR) values are evaluated to confirm the antenna's safety against harmful electromagnetic radiation. Finally, as part of the application scope, Section 2.4 evaluates the practical on-body communication performance of the proposed SWB HSA using simulated two-antenna S_{21} on a voxel phantom and link-budget analysis across two representative mmWave scenarios.

2.1. Design and analysis

In this section, the design procedure is presented step by step. Step 1 explains the creation of the Hilbert curve, outlining how its fractal geometry is generated. Step 2 focuses on designing the HSA using the design equations corresponding to the required operating frequency. Also, it discusses how the design is evaluated and optimized to achieve the optimal dimensions that ensure good performance. Finally, Step 3 presents the parametric studies conducted on the optimized design from Step 2 to further enhance compactness and overall performance.

Step 1: Fractal Geometry Generation

Obtaining a Hilbert curve with $n > 1$ increases the electrical length while maintaining the external dimensions, resulting in increased electrical compactness. It is akin to using a meandering line, but the different segments corresponding to the iterations excite more resonances, leading to multi-band operating frequencies and a wider BW. According to [33,34], the Hibert curve can be obtained by first dividing the unit square into four sub-squares with half the side length of the main square. Then, a space-filling curve should be created for each sub-square by scaling down, rotating, or reflecting the original curve, where the respective reflection and rotation operations are to be chosen such that the four partial curves can be connected in a way to preserve continuity. The creation of the Hibert curve is illustrated in Fig. 1, starting from the unit square ($n = 1$). The study in [32] showed that increasing the fractal iteration improves multi-band performance and shifts the resonant frequency higher, while reducing return loss.

Step 2: Initial Design and Optimization

To design an antenna based on the Helbert curve, the dimensions of the curve include the side length L_S (a fixed external dimension) and are based on the operating frequency. We can first consider a square patch antenna with L_s length, so at (24–64 GHz), and based on the Microstrip patch antenna online calculator [35], L_s is approximately equal to 2 mm.

The length of each line segment L_L for the third iteration, $n = 3$, can be calculated using the following equation.

$$L_L = L_S/1 + 2^n \tag{1}$$

Which is approximately equal to 0.22 mm. It should be noted that we chose the cell thickness T_S to be equal to L_S for greater compactness. L_L plays a crucial role in controlling the operating frequency band, where small changes in its value result in a dramatic shift, as will be explained later in parametric studies.

The layouts of the HSA at $n = 3$ and $n = 4$, along with their performance, are illustrated in Fig. 2. Cases 1 and 4 in Fig. 2(a), are referred to the slot antenna based on the 4th and 3rd order inverted Hilbert curve, respectively, while Cases 2 and 3 are referred to the slot antenna based on the 4th order inverted Hilbert curve with three and two segments. It should be noted that lower fractal order ($n = 3$) inherently reduces geometrical complexity and fabrication effort compared to higher fractal order. Case 5 refers to the slot antenna based on a 4th-order normal (non-inverted) Hilbert curve (as shown in the inset of Fig. 2(b)). The inverted Hilbert curve is selected in this work for its superior performance and convenient placement of the feed line, as shown in Fig. 2(b) and (c) by comparing Case 1 ($S_{11} < -8.85$ at 33.92– 65.51 GHz, BW=31.59 GHz and maximum gain (MG) = 6.57 dBi) with Case 5 ($S_{11} < -8.71$ dB at 35.72– 59.36 GHz, BW=23.64 GHz and MG = dBi). Although Case 1 provides wide BW however, its lower frequency band falls outside the FR2 range. As shown form the result, Case 4 ($S_{11} <$

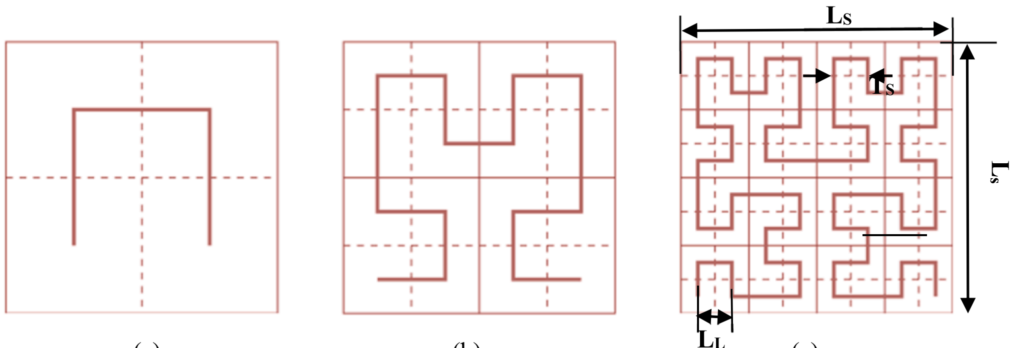

(a) (b) (c)

Fig. 1. Geometry of Hilbert curve (a) $n = 1$, (b) $n = 2$ and (c) $n = 3$ [34].

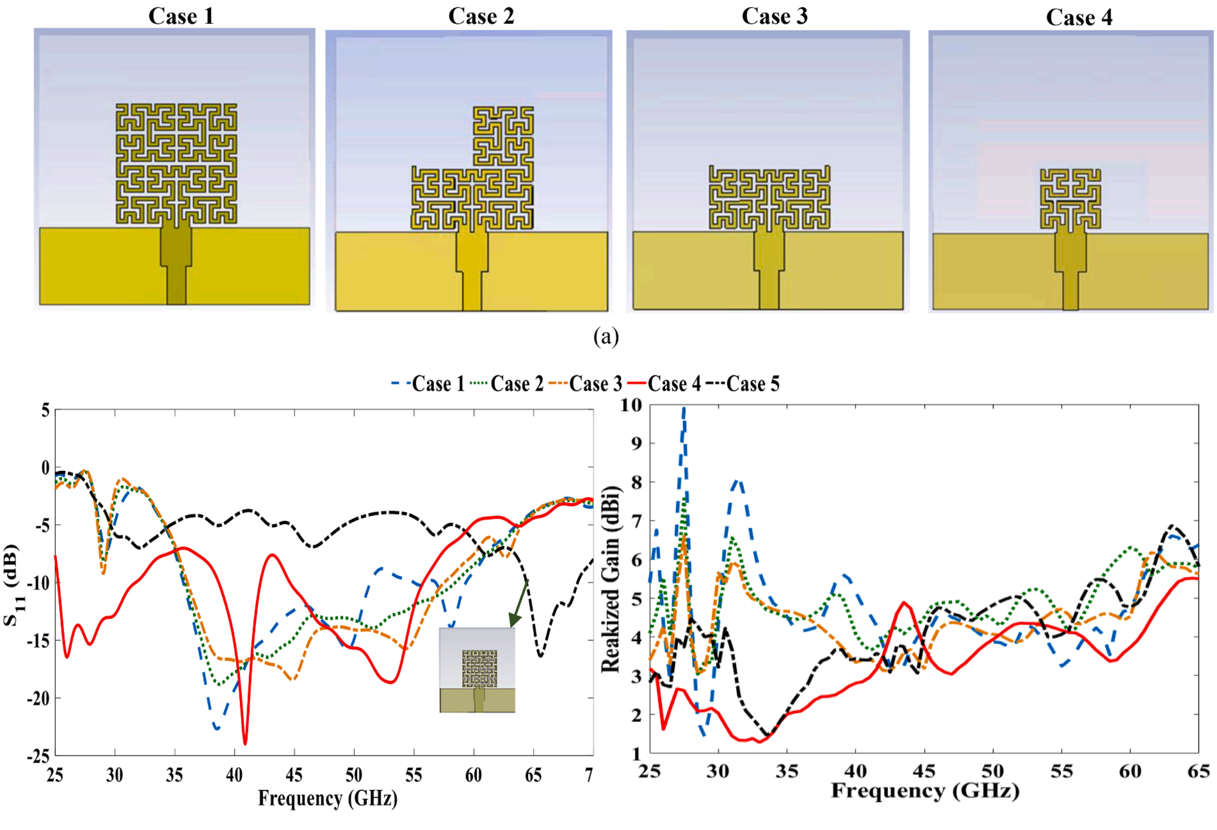

(a)

(b) (c)

Fig. 2. (a) Design evolution for Hibert-based antenna with different iterations and segments (a), (b) Simulated S_{11} and (b) Simulated gain.

−7.16 dB at 25.25– 55.62 GHz, BW=30.37 GHz and MG = 4.90 dBi) with its small size provide 19%, 25.52%, 22.16% wider BW than Case 2 ($S_{11} < -13.85$ dB at 34.87– 59.47 GHz, BW=24.6 GHz and MG =6.14 dBi), Case 3 ($S_{11} < -12.80$ dB at 35.84– 58.46 GHz, BW=22.62 GHz and MG = 4.70 dBi) and Case 5 ($S_{11} < -8.71$ dB at 35.72– 59.36 GHz, BW=23.64 GHz and MG = 5.48 dBi), respectively. Compared to the $n = 4$ configurations, the $n = 3$ Hilbert geometry significantly reduces design complexity while maintaining wideband characteristics. This compact design makes the antenna an excellent choice for wearable applications, where compactness and compatibility are essential for user comfort. Additionally, it serves as a promising building block for MIMO systems, providing wide and reliable coverage for WBAN communication. Additionally, the reduced fractal order simplifies the antenna geometry, which is advantageous for fabrication scalability and future MIMO integration. For more details, Table 2 illustrates the trade-off analysis for the different cases in terms of matching. BW, gain and structure complexity.

It should be noted that the partial ground is used to get enhanced performance in terms of matching and BW, which will be explained in the following paragraph, optimizing the antenna's primary dimension and parameters.

It should be mentioned that substrate modes are particularly significant in mmWave designs due to the thin dielectric substrate and high operating frequencies. These modes can lead to unwanted surface-wave propagation, degrading impedance matching, radiation efficiency, and bandwidth. Techniques such as partial ground planes and optimized slot geometries are commonly used to suppress substrate/surface waves in high-frequency antennas, thereby improving wideband performance, minimizing unwanted resonances, and stabilizing radiation characteristics [36]. To improve the gain and BW in Case 4 ($n = 3$), some

Table 2
Multi-objective comparison of different fractal orders for HSA.

Case	Fractal Order (n)	S_{11} (dB) at Frequency Band (GHz), BW (GHz)	MG (dBi)	Structural Complexity
Case 1	$n = 4$ (Inverted)	$S_{11} < -8.85$ at 33.92–65.51, 31.59	6.57	medium
Case 2	$n = 4$ (Inverted with three cells)	$S_{11} < -13.85$ at 34.87–59.47, BW=24.6	6.14	medium
Case 3	$n = 4$ (Inverted with two cells)	$S_{11} < -12.80$ at 35.84–58.46, 22.62	4.70	medium
Case 4	$n = 3$ (inverted)	$S_{11} < -7.16$ at 25.25–55.62, 30.37	4.90	low
Case 5	$n = 4$ (non-inverted)	S11< −8.71 dB at 35.72– 59.36, 23.64	5.48	
Case 6	Case 4 with stand position	$S_{11} < -10.23$ at 26.32–59.30, 32.98 GHz	7.05	
Case 7	Case 6 with slot	$S_{11} < -14.64$ at 26.11–60.40, 34.29	6.32	
Case 8	Case 7 with extension	$S_{11} < -10$ at 26.25–63.31, 37.07 GHz	6.38	
Case 9	Optimized Case 8	$S_{11} < -12.18$ at 24.66–62.59, 37.93	7.35	

modification is added to the radiating patch, feed and matching lines resulting in final layout (Case 9) as shown in Fig. 3. Firstly, the stand position is modified to improve the matching (Case 6: $S_{11} < -10.23$ dB at 26.32–59.30 GHz, BW = 32.98 GHz and MG = 7.05 dBi), as shown in Fig. 4. Then, the slot is etched in the matching line (Case 7), resulting in improved matching and bandwidth (Case 7: S11 < −14.64 dB at 26.11–60.40 GHz, BW = 34.29 GHz and MG = 6.32 dBi). An additional 2.78 GHz of BW improvement is achieved in Case 8 ($S_{11} < -10$ dB at 26.25–63.31, BW=37.07 GHz and MG = 6.38 dBi) and MG = dBi is obtained by adding external line to one side of the radiating patch. Finally, an improvement in matching and BW compared to Case 8, is obtained by adding the second external line to the patch resulting in Case 9: $S_{11} < -12.18$ dB at 24.66–62.59 GHz, BW = 37.93 GHz and MG = 7.35 dBi).

Step 3: Parametric Analysis and Performance Enhancement

Now, for more performance improvement, a parametric study is performed on the final layout (Case 9 shown in Fig. 3 where *Subx, Suby, Gndy,* L_f, W_f, L_m, W_m, L_{sl}, W_{sl}, *extl, extw,* and *g* are the substrate length in x-direction, the substrate length in y-direction, the ground plane length in y-direction, feedline length, feedline width, matching line length, matching length width, slotline length, slotline width, extension length, extension width, and gap between the segments. As shown, two stands are used to fix the position of the two bottom segments on the matching line. The final optimized dimensions of the selected single element (Case 9) in Fig. 3 are obtained based on the parametric studies in Table 3 and Fig. 5 in terms of S_{11} and gain.

Table 3 and Fig. 5 illustrate the effect of changing the parameters on the antenna performance in terms of S_{11} and gain. The value of L_L has a significant impact on the operating frequency, as shown in Table 3 and Fig. 5(a). The calculated values of 0.22 mm and 0.2 mm result in a significant shift to the operating frequencies of 20.11 GHz and 22.11 GHz, respectively. As illustrated in Table 2 and Fig. 5(b), $L_f = 1$ mm is selected due to its better matching than $L_f = 0.8$ mm. Although the BW obtained by $L_f = 1$ mm is only 0.76% wider than the BW obtained by $L_f = 1.2$ mm, it is selected due to the compactness. As illustrated in Table 3 and Fig. 5 (c), $W_f = 1.75$ mm is selected due to its better matching within the required band compared to 1.65 mm and 1.85 mm. Although the BW at $W_f = 1.85$ is broader than that at 1.75 mm, it is selected for its better matching. Table 3 and Fig. 5(d) illustrate that although the matching, BW, and maximum gain (MG) at $L_m = 1.2$ mm are better than 1 mm, it is selected for more compactness. As depicted in Table 2 and Fig. 5(e), $W_m = 1.4$ mm yields a better matching and BW than $W_m = 1.2$ mm and 1.6 mm, respectively. For better matching, BW and gain, as shown in Table 3 and Fig. 5(f-g), the slotline length, $L_{sl} = 0.95$ mm, and the slotline width, $W_{sl} = 0.8$ mm are selected. As illustrated in Table 3 and Fig. 5 (h-i), adding the extension helps improve the matching and gain, with the best values of *extl* = 0.2 mm and *extw* = 0.8 mm. For improved BW, the partial ground length is selected to be *Gndy* = 2 mm as shown in Table 3 and Fig. 5(j). As illustrated in Table 3 and Fig. (k-l), *Subx*= *Suby*= 7.31 mm is selected for more compactness with better matching and BW. In terms of gain in Fig. 5, we can notice that it is decreasing at certain high-frequency bands, which can be attributed to increased dielectric losses in the substrate or higher conductor losses and impedance mismatch away from primary resonant modes. After those, higher-order modes or optimized modal structures can recover gain. This behavior is consistent with recent findings in wideband and metasurface antenna literature [37,38]. The fabricated prototype of the proposed SWB HSA based on the optimized parameters is illustrated in Fig. 6.

To understand the gain behavior observed in Fig. 7, the surface current distribution at various frequencies for the final optimized layout (Case 9) is analyzed. It is worth noting that the color map in Fig. 8 represents the real current magnitude values (A/m), not a normalized or logarithmic scale. Therefore, regions shown in lighter colors still correspond to strong current intensities, indicating that the current is indeed well distributed across the Hilbert structure, even though the visual contrast might suggest otherwise.

As shown in Fig. 8(a), the surface current at a lower frequency (30 GHz) is less concentrated and distributed sparsely along the Hilbert slot edges. This results in relatively low gain (as shown in Fig. 7) due to

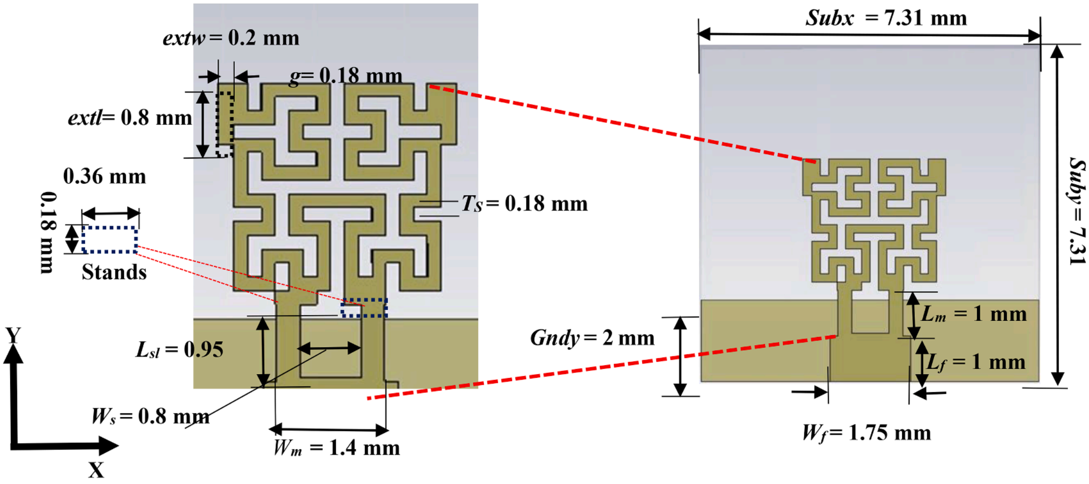

Fig. 3. Layout of the proposed 5 G mmWave (FR2) 3rd order SWB HSA.

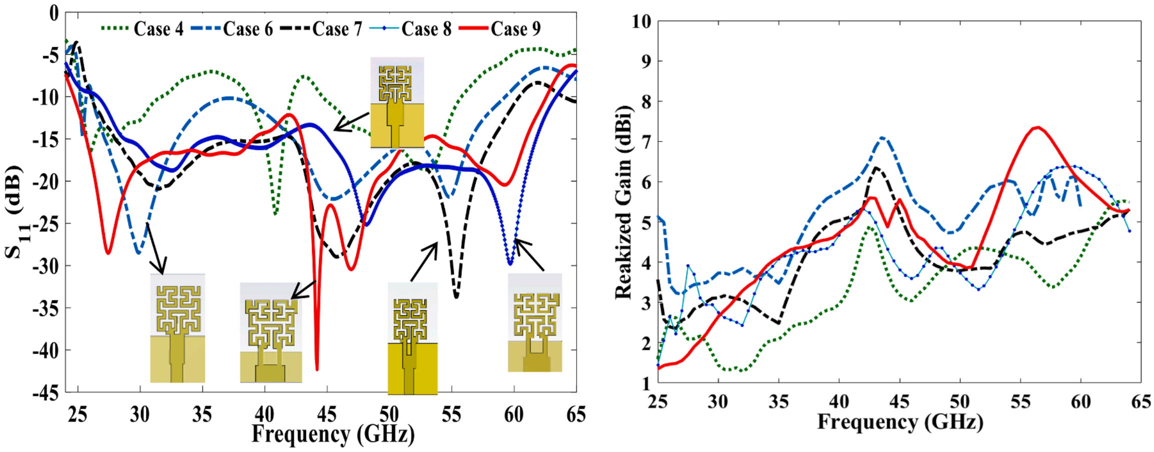

(a)

(b)

Fig. 4. Design evaluation for the proposed 5 G mmWave (FR2) 3rd order SWB HAS: (a) Simulated S_{11} and (b) Simulated gain.

Table 3
Parametric study of Case 9.

Par.	Parameter value (S_{11}(dB), Frequency Band (GHz), MG (dBi))		
L_L	**0.18(<−12.18, 24.66– 62.59 = 37.93,7.35)**	0.2(<−9.64, 22.31– 56.59=34.28,6.91)	0.22(<−6.11, 20.11–60.51=40.4,6.28)
L_f	0.8 (<−11.41, 24.68–62.66=37.98,7.16)	**1 (<−12.18, 24.66– 62.59=37.93,7.35)**	1.2(<−13.05, 24.68–62.32=37.64,7.44)
W_f	1.65 (<−13.87, 25.14–62.53=37.39,7.41)	**1.75 (<−12.18, 24.66– 62.59=37.93,7.35)**	1.85(<−11.79, 24.61–61.35=38.01,7.33)
L_m	0.8 (<−10.33, 24.74–63.22=38.48,7.02)	**1 (<−12.18, 24.66– 62.59=37.93,7.35)**	1.2(<−13.35, 24.73–61.85=37.12,7.52)
W_m	1.2 (<−9.8, 24.73–63.15=38.41,7.35)	**1.4(<−12.18, 24.66– 62.59=37.93,7.35)**	1.6(<−12.14, 25.32–61.35=36.03,7.43)
L_{sl}	0.75 (<−11.51, 24.73–62.50=37.77,7.29)	0.85 (<−11.99, 24.73–62.54=37.81,7.31)	**0.95 (<−12.18, 24.66– 62.59=37.93,7.35)**
W_{sl}	0.7 (<−10.98, 24.87–61.81=36.94,7.43)	**0.8 (<−12.18, 24.66– 62.59=37.93,7.35)**	0.9(<−12.15, 24.63–62.5 = 37.87,7.32)
extl	0 (<−11.48, 24.86–63.92=39.06,7.17)	**0.2(<−12.18, 24.66– 62.59=37.93,7.35)**	0.4(<−12.05, 24.65–62.01=37.36,6.56)
extw	0.6 (<−10.67, 28.15–66.04=37.89,6.81)	**0.8 (<−12.18, 24.66– 62.59=37.93,7.35)**	1(<−13.74, 25.29–63=37.71,7.51)
Gndy	1.8 (<−5.16, 27.91–62.6 = 34.99,7.53)	**2 (<−12.18, 24.66– 62.59=37.93,7.35)**	2.2(<−8.24, 25.98–62.52=36.54,7.56)
Subx	7.13 (<−11.74, 24.76–62.68=37.92,7.3)	**7.31 (<−12.18, 24.66– 62.59=37.93,7.35)**	7.49(<−13.05, 24.59–62.44=37.85,7.35)
Suby	7.13 (<−12.16, 24.70–62.52=37.82,7.3)	**7.31 (<−12.18, 24.66– 62.59=37.93,7.35)**	7.49(<−12.17, 24.7–62.57=37.87,7.37)

weaker radiation efficiency caused by incomplete current alignment with the radiating slots. In Fig. 8(b)–(d), as the frequency increases (34–48 GHz), the current distribution begins to align more effectively along the slot edges and the feeding structure. Increased current density and stronger resonance result in a gradual improvement of gain. The current distribution expands to the upper segments of the Hilbert structure, enhancing resonance and improving gain, which reaches values between 5.10 dB and 5.88 dB as shown in Fig. 7.

Fig. 8(e-f) shows that, as the frequency increases to the mid-range (46– 52 GHz), the average surface current magnitude gradually decreases from 152 A/m at 42 GHz to 128 A/m at 46 GHz, and further to 121 A/m at 52 GHz. This reduction in current indicates weaker excitation of the radiating slots, which contributes to the observed 1.5 dB gain drop in the mid-frequency range. Minor impedance mismatches and dielectric losses in this frequency band further reduce radiation efficiency. At higher frequencies (54 – 58 GHz), as shown in Fig. 8(g) and (h), the surface current effectively utilizes the entire Hilbert structure, including the higher-order segments and extended slots. This uniform current distribution minimizes losses and enhances radiation efficiency, resulting in peak gain values ranging from 6.22 dB to 7.35 dB. While current density remains high beyond the 58 GHz (e.g., 62 GHz) as depicted in Fig. 8(i), the effects of surface current losses, slight mismatches, or substrate limitations begin to reduce gain slightly. It explains the observed decline in gain at higher frequencies [37,38]. Thus, both the ~1.5 dB drop in the mid-frequency range and the decline at higher frequencies are primarily due to the combined effects of weaker current excitation, impedance mismatches, and material losses, rather than any structural defects.

The compact Hilbert-based geometry, combined with a partial ground plane, optimizes current flow and impedance matching, enabling consistent performance across a wide BW (24.66–62.59 GHz). This highlights the antenna's efficiency, making it a strong candidate for 5 G mmWave applications.

2.2. Bending and on-body performance

Since the proposed wearable antenna is fabricated on a semi-flexible substrate (Rogers RT/Duroid 5880 with a thickness of 0.501 mm), it is essential to test its bending performance to ensure resistance to external mechanical forces. Therefore, the proposed SWB HSA is bent along the x-axis at three different bending radii ($R = 40$ mm, 30 mm, and 20 mm), as shown in Fig. 9(a). Fig. 9(b) illustrates the impact of x-axis bending on the S_{11} compared to the flat surface. The 40 mm bent prototype prepared for measurement is shown in the inset of Fig. 9(b). As seen in Fig. 9(b), bending has a more significant effect when the curvature radius is smaller: at $R = 20$ mm ($S_{11} < -9.22$, $26.63–62.07 = 35.44$ GHz) and $R = 30$ mm ($S_{11} < -9.04$, $26.96–61.86 = 34.90$ GHz), where slight mismatches occur within the required frequency band. However, at $R = 40$ mm (Sim: $S_{11} < -10.34$, $23.98–61.71 = 37.73$ GHz and Meas.: $S_{11} < -10$, 24–62.00= 38 GHz), the antenna still achieves matching within the desired frequency band. It should be noted that the slight losses observed in the measurements are attributed to the use of the standard 1.85 mm coaxial connector with an attached cable (as shown in the inset of Fig. 9(B). In future studies, to further minimize such losses, dedicated 5 G SMA connectors (2.4 mm) will be employed. These results demonstrate the antenna's robustness against mechanical forces within certain limits, due to its semi-flexible material. For improved robustness and flexibility, future work will explore the use of fully flexible fabric or

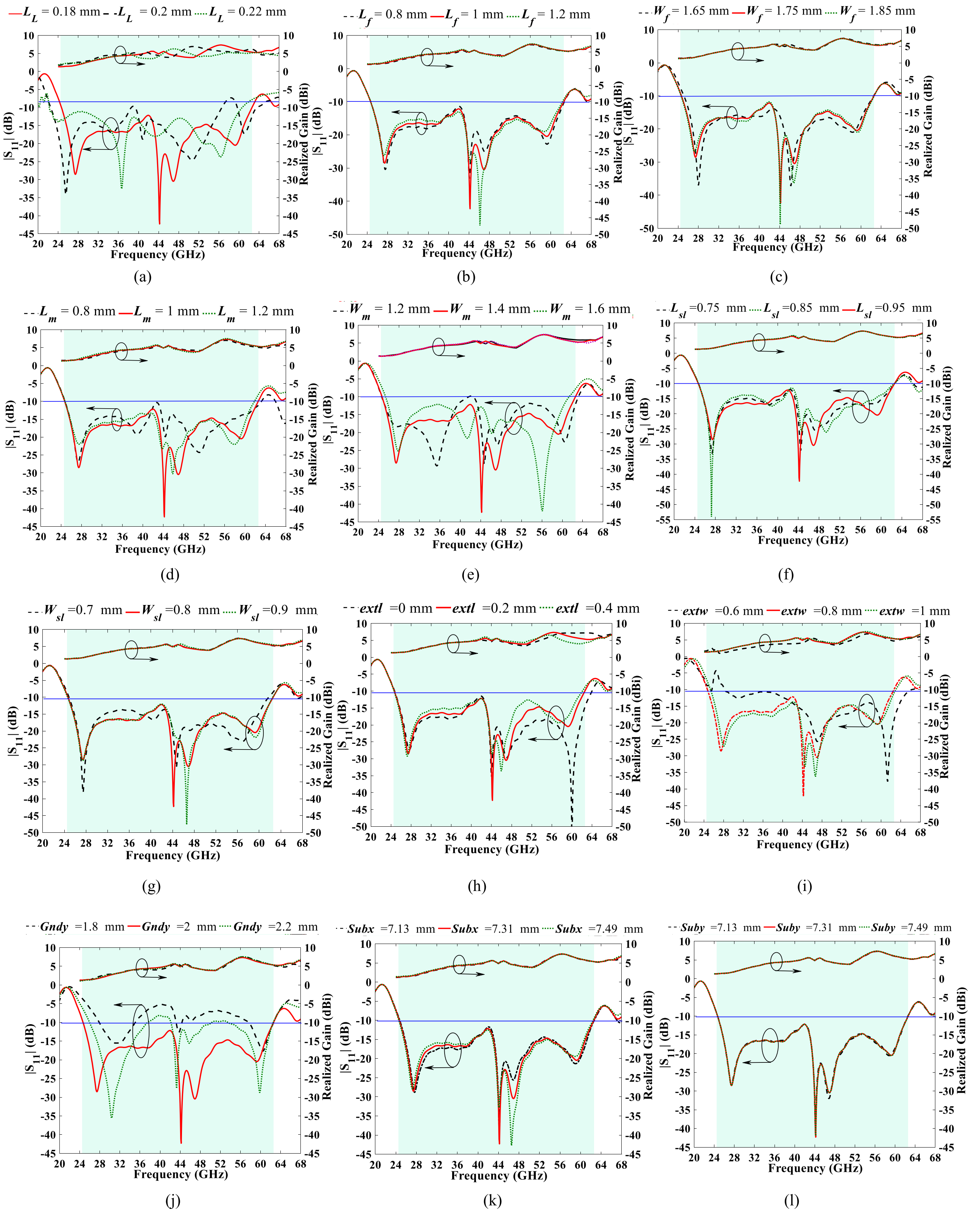

(a) (b) (c)

(d) (e) (f)

(g) (h) (i)

(j) (k) (l)

Fig. 5. S_{11} and gain parametric study on (a) *ut*, (b)L_f, (c)W_f, (d)L_m, (e)W_m, (f)L_{sl}, (g)W_{sl}, (h) *extl*, (i)*extw*,(j) *Subx*, (k)*Suby*, and (l) *Gndy* for the compact SWB HSA.

non-fabric materials.

To ensure the antenna's efficiency for wearable applications, its performance must be evaluated close to the human body, where the high dielectric properties of tissues significantly impact its behavior. Firstly, and based on [39], the proposed antenna was positioned 10 mm away from a cylindrical human phantom including skin, fat, and muscle, as illustrated in Fig. 10(a). It should be noted that the phantom was viewed in an angular view for clear vision [40,41]. To make the antenna more durable, it was bent with radii of 20 mm and 30 mm and then compared to a flat one and a free space. Table 4 provides details on the dielectric

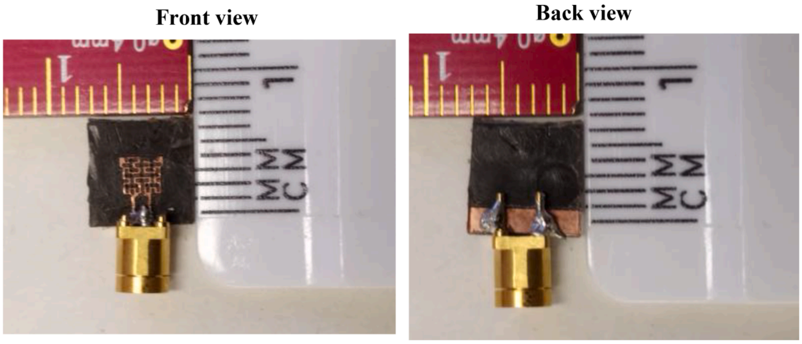
Front view

Back view

Fig. 6. Prototype of the compact SWB HSA.

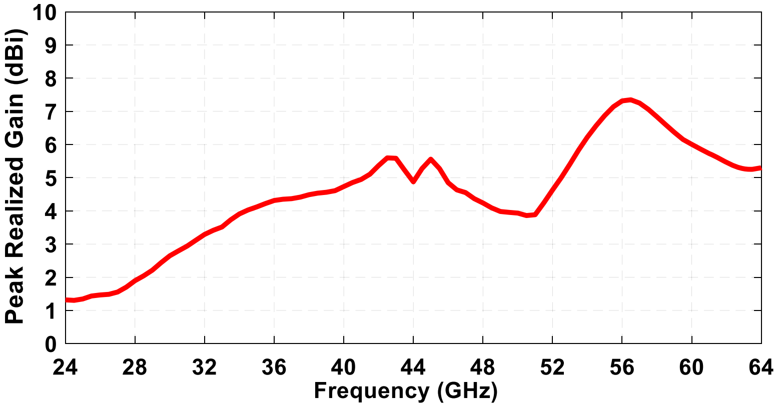

Fig. 7. Simulated gain for the proposed compact SWB HSA.

characteristics of various tissues at lower frequencies, including mass density, relative permittivity (εr), conductivity, and thickness. When the antenna was placed on the cylindrical phantom without bending (flat), as shown in Fig. 10(b), the frequency shifted and there was a slight mismatch, but the BW was wider ($S_{11} < –9.63$ dB, 23.65–64.85 GHz = 41.2 GHz) than in the free-space case ($S_{11} < –12.18$ dB, 24.66–62.59 GHz = 37.93 GHz and this related to the effect of high dielectric tissues. In addition to the effect of the human tissues on the antenna performance, the figure also demonstrates that at lower curvature radii, like $R = 30$ mm ($S_{11} < –9$ dB, 24.01–60.74 GHz = 35.44 GHz), bending has a more noticeable effect on impedance matching and BW. On the other hand, less influence is produced by a higher curvature radius, such as $R = 40$ mm ($S_{11} < –9.65$ dB, 23.98–61.71 GHz = 37.73 GHz). Secondly, the antenna was placed 10 mm away from the arm, shoulder, and chest of the CST-based Gustav phantom body model, as shown in Figs. 11(a), 11(b), and 11(c), respectively. The impact of this configuration compared to the free-space case is illustrated in Fig. 12. Due to the high dielectric tissues, the antenna matching at the arm (Sim.: $S_{11} < −8.93$ dB, 23.03–63.09 GHz = 40.06 GHz. Meas: $S_{11} < −8.86$ dB, 23.86–63.72 GHz = 39.86 GHz), shoulder ($S_{11} < −9.06$ dB, 23.95–65.17 GHz = 41.22 GHz. Meas: $S_{11} < −8.93$ dB, 23.03–63.09 GHz = 40.06 GHz), and chest (Sim.:$S_{11} < −8.520$ dB, 23.50–65.73 GHz = 42.23 GHz. Meas: $S_{11} < −9.02$ dB, 24.05–63.56 GHz = 39.06 GHz) is degraded by 3.25 dB (Meas. 3.12: dB),),12 dB (Meas.3.25: dB), and 3.64 dB (Meas.3.16: dB), respectively, with increasing BW of 2.13 GHz, 3.29 GHz, and 4.3 GHz, respectively as shown in Fig. 12. These results demonstrate that, despite the degradation in antenna matching due to the influence of the lossy body tissues [42], the proposed antenna remains functional within the desired frequency range, confirming its applicability for wearable applications. The increased BW in proximity to the body further supports the feasibility of this antenna design in practical, wearable scenarios.

Table 5 illustrates the investigation of linear 3D and nonlinear 2D radiation patterns at different frequencies to further assess the antenna's performance in body-worn scenarios. The antenna primarily radiates outward, avoiding alignment parallel to the body surface, where destructive cancellation from body coupling typically occurs, as indicated by the 3D radiation patterns observed in voxel, cylindrical, and free-space phantoms. Even at high mmWave frequencies, the results indicate minimal pattern distortion and stable radiation characteristics. These results give a comprehensive view of the antenna’s behavior, establishing it as a strong candidate for reliable and safe wearable communication systems [16,42]

2.3. SAR calculation

To ensure protection from potentially hazardous electromagnetic radiation, the SAR (Specific Absorption Rate) values for the proposed FR2 antenna on the arm, shoulder, and chest of the CST-based Gustav phantom body model and the cylindrical phantom were calculated at different frequencies, as shown in Fig. 13, Fig. 14, Fig.15, and Fig. 16, respectively. The SAR values, which were determined using an input power of 100 mW (20 dBm) over 1 g and 10 g masses of actual tissue, were well below the safety limits set by the European Union, EU, (<2.0 W/kg averaged over 10 g) and the Federal Communications Commission, FCC, (<1.6 W/kg averaged over 10 g). Table 6 compares the SAR results for the different phantoms at these frequencies, where these thresholds confirming their safe operation for wearable applications.

Based on the SAR distribution maps presented in Figs. 13–16 and the quantitative data summarized in Table 6, it can be concluded that antenna placement and operating frequency significantly influence the SAR values. the lowest SAR values are observed on the arm across the

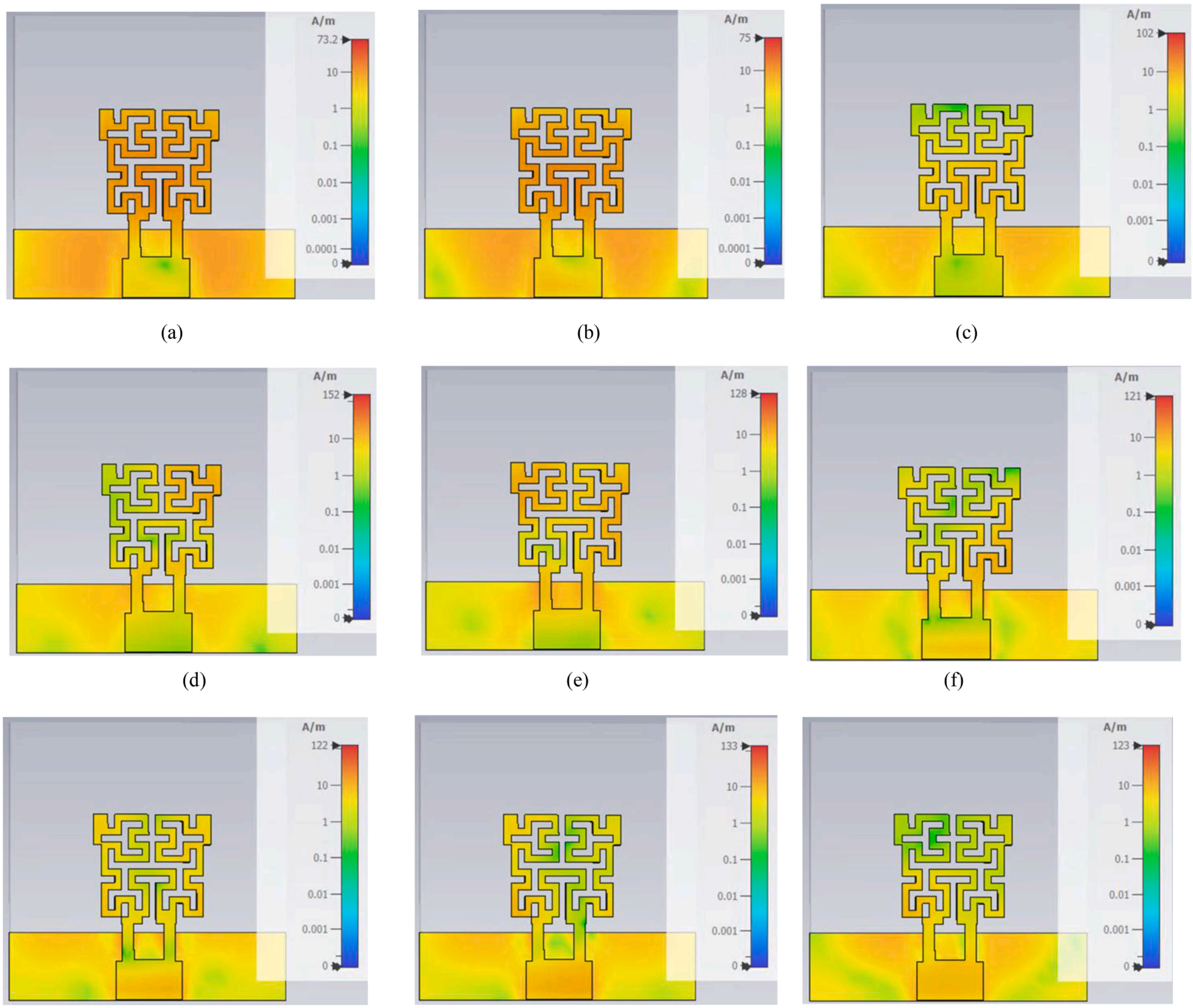

(a) (b) (c)

(d) (e) (f)

(g) (h) (i)

Fig. 8. Simulated surface current distribution for the proposed compact SWB HSA at (a) 30 GHz, (b) 34 GHz, (c) 38 GHz, (d) 42 GHz, (e) 46 GHz, (f) 50 GHz, (g) 54 GHz, (h) 58 GHz, and (i) 62 GHz.

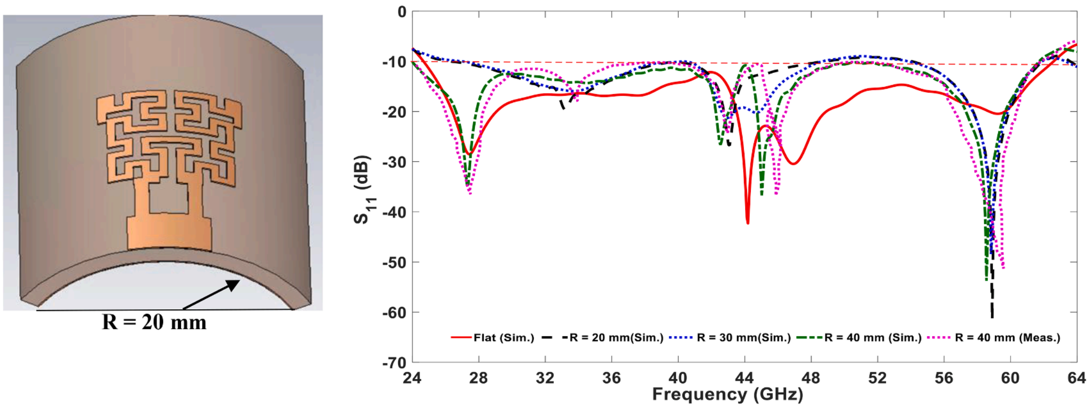

(a) (b)

Fig. 9. (a) Layout and (b) S_{11} response of the proposed compact FR2 HSA under bending along the x-axis.

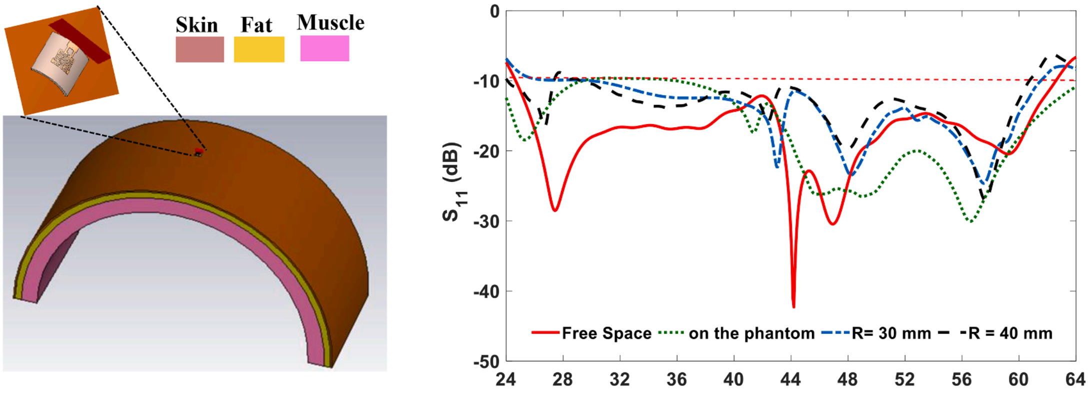

(a)

(b)

Fig. 10. (a) The FR2 HSA on the on the cylindrical phantom and (b) the resulting simulated S_{11}.

Table 4
Densities and electric properties of the phantom tissues.

Parameters	Skin	Fat	Muscle
Mass density (Kg/m3)	1090	950	1040
ε_r	18.6	6.43	26.9
conductivity (S/m)	23.4	4.53	30.2
Thickness (mm)	2	10	20

entire frequency range, particularly above 38 GHz, due to increased surface curvature and reduced effective antenna–tissue coupling. Slightly higher SAR levels are illustrated on the shoulder, attributed to thicker muscle layers and reduced curvature, while the chest exhibits comparatively lower SAR at higher frequencies as a result of increased antenna–body separation and enhanced field spreading.

In contrast, the cylindrical phantom generally produces higher SAR values because of its simplified geometry and continuous tissue contact, which lead to stronger electromagnetic coupling, as clearly visible in the corresponding SAR maps. Moreover, for all investigated configurations, the SAR level decreases with increasing frequency, which is consistent with the reduced penetration depth of mmWave signals and stronger near-surface field confinement. These observations indicate that arm-mounted wearable configurations are particularly favorable for prolonged operation, while all evaluated scenarios remain well within international SAR safety limits.

2.4. *Application scope*

To evaluate practical on-body communication performance, we used the simulated two-antenna transmission coefficient S_{21} (port-to-port)

(a)

(b)

(c)

Fig. 11. Positioning of the proposed compact FR2 HAS on the CST-based Gustav phantom body model: (a) Arm, (b) Shoulder, and (c) Chest.

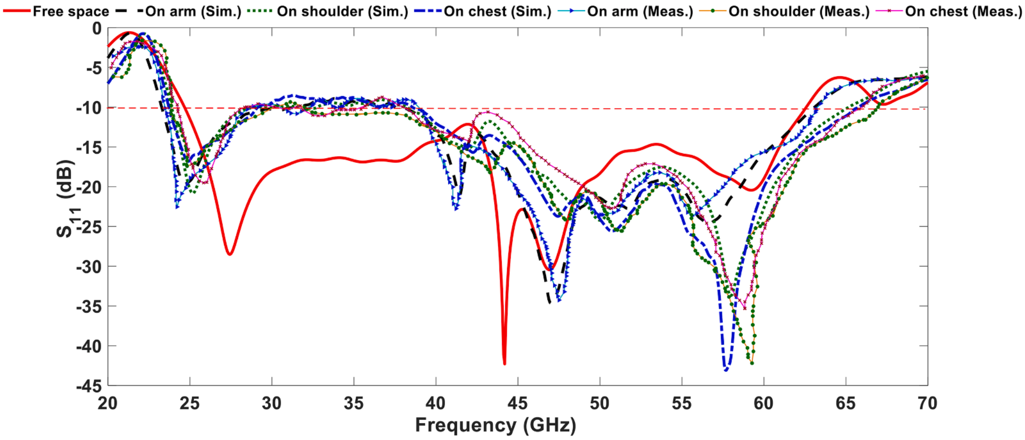

Fig. 12. Comparison of the S_{11} parameter of the proposed compact FR2 HSA in proximity to the arm, shoulder, and chest (voxel model) with the free-space case.

Table 5

Nonlinear 3D and linear 2D radiation patterns of the proposed antenna on the Gustave and cylindrical phantom.

Freq. (GHz)	Voxel (arm)	Voxel (shoulder)	Voxel (chest)	Cylindrical phantom
25	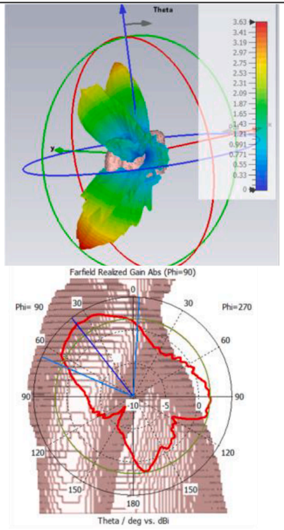	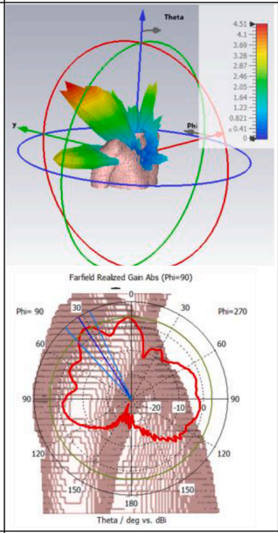	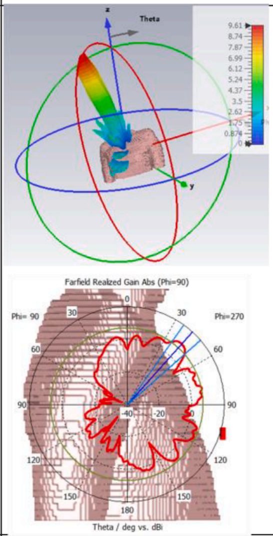	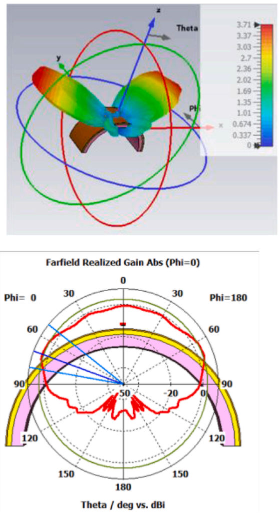
28	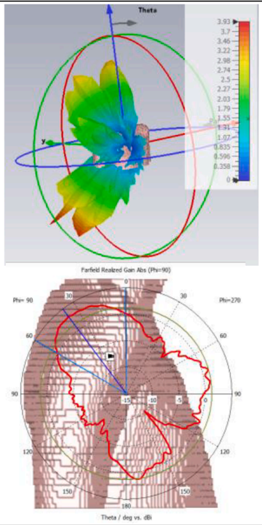	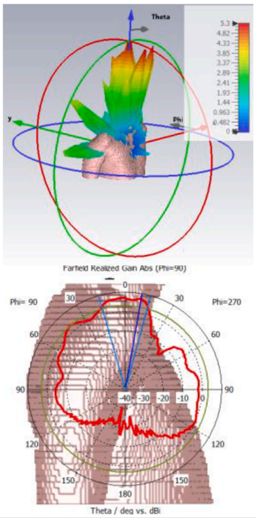	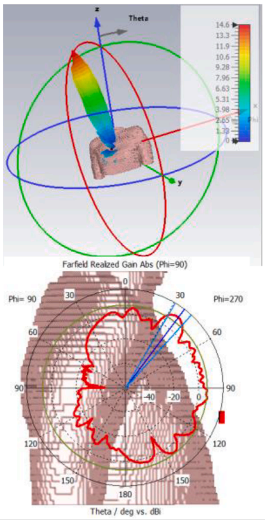	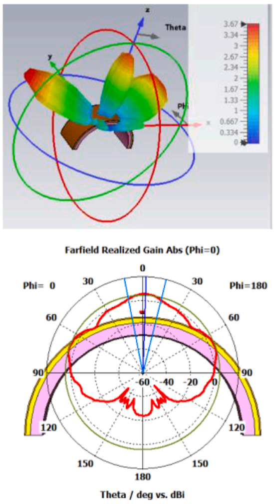

(*continued on next page*)

Table 5 (*continued*)

38	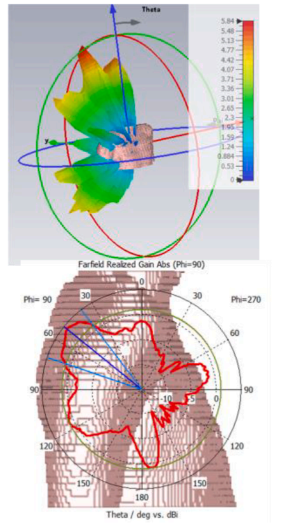	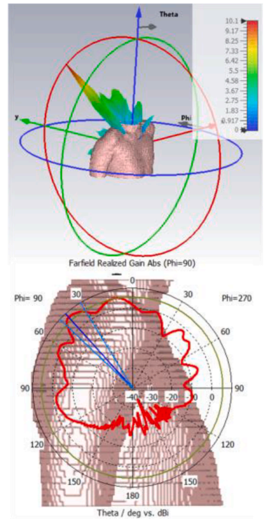	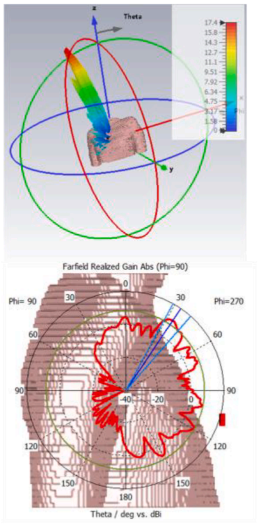	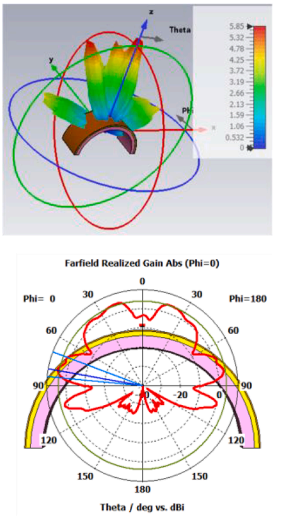
47	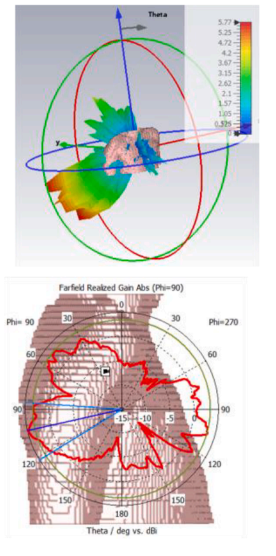	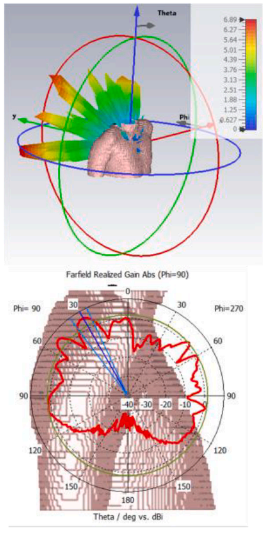	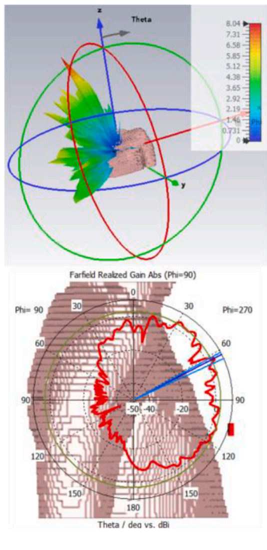	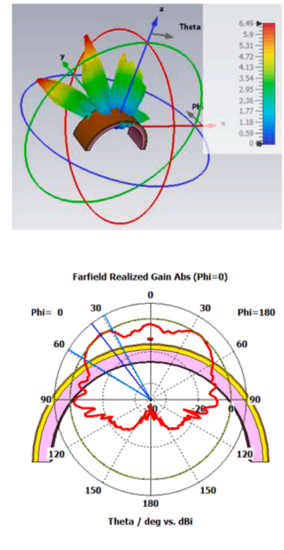
50	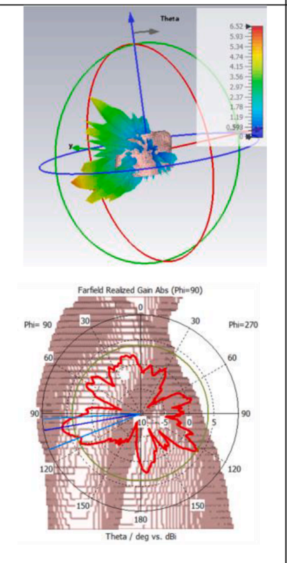	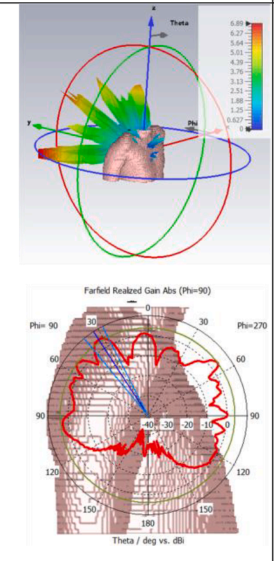	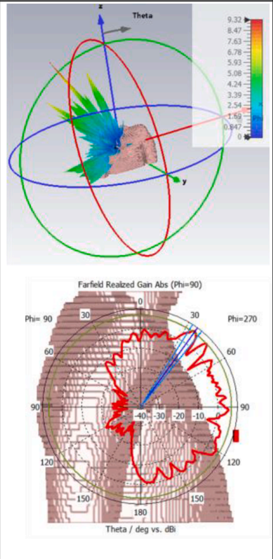	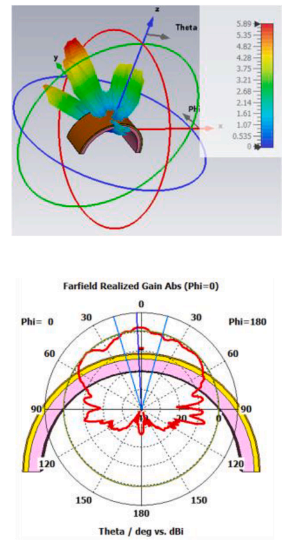

(*continued on next page*)

Table 5 (*continued*)

57	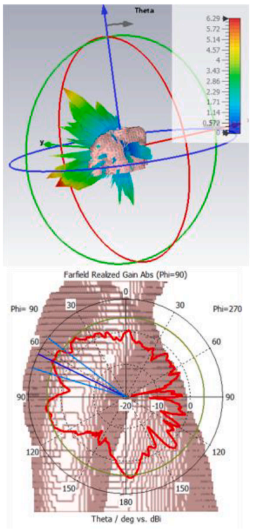	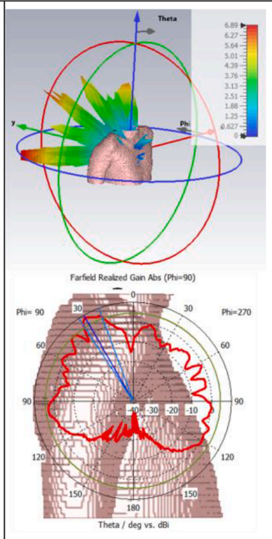	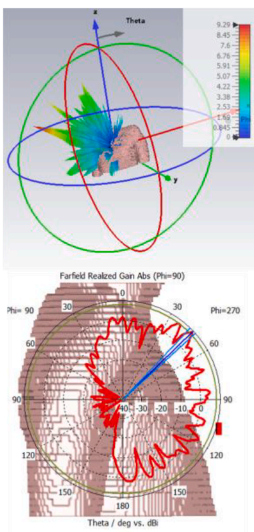	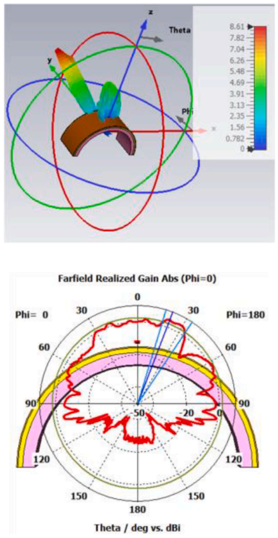
60	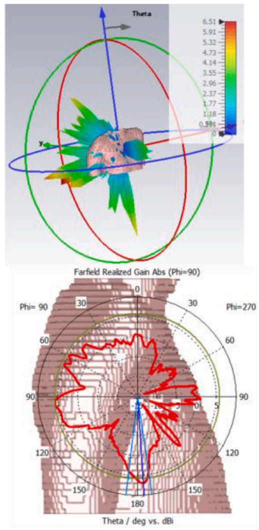	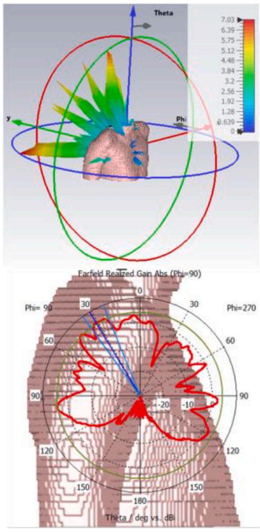	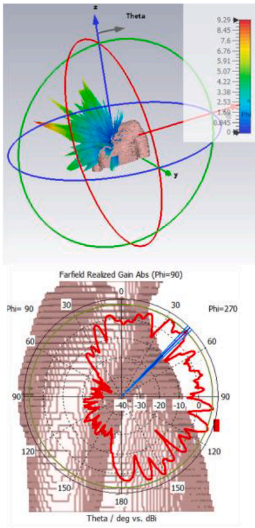	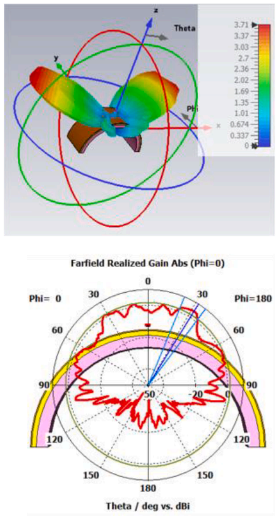

calculated on the voxel phantom as the channel transfer function. As shown in Fig. 17(a), two antennas are used one on the shoulder and other on the chest. The received power (Pr) is calculated as

$$Pr = Pt + S_{21}(dBm) \tag{2}$$

The link margin (LM) can be obtained using:

$$LM = \mathrm{Pr} - (N + SNR) \tag{3}$$

$$N = -174 + 10\log_{10}(B) + NF \tag{4}$$

Where SNR is the signal-to-noise ratio, N is the noise, and NF is the noise floor, which can be computed from thermal noise, $N_0 = -174$ dBm/Hz, and it is scaled by the chosen channel bandwidth (B) and NF

So to calculate the LM, we are considering two scenarios: The first one is the wearable/low-power scenario (Scenario A), where Pt=0 dBm, NF = 6 dB, required SNR = 10 dB, and $B = 100$ MHz. Whereas in the second scenario (Scenario B), a high-rate short-range is considered with Pt=+10 dBm, NF = 4 dB, required SNR = 6 dB, and $B = 1$ GHz. These parameter choices are typical for wearable/body-area research and short-range mmWave links [43–45]. The resulting LM (in dB) versus frequency (in GHz) is illustrated in Fig. 17(b), which improves communications robustness across the antenna's operating band. Fig. 17(b) shows that the proposed SWB HSA provides positive LM across most of its operating band, with larger margins observed in the mid-band where S_{21} is strongest. The Notable dips in the figure correspond to frequencies where S_{21} has deeper minima. For Scenario A, link margins are typically well above 0 dB across the key mmWave range, indicating that the antenna and on-body channel provide sufficient received power for reliable communications under typical wearable transmitter power and receiver noise figures. In Scenario B, margins are even higher, confirming suitability for higher throughput short-range links. Overall, these link-budget results confirm that the antenna's wide operating band and on-body S_{21} performance translate into robust communication margins for realistic wearable IoT use cases (e.g., health patches, body area networks, and short-range wearable links).

3. Experimental validation and discussion of results

The proposed compact SWB HSA was fabricated using the LPKF ProtoMat S104 [46], a high-precision PCB milling machine specifically designed for rapid prototyping of RF and microwave circuits. This machine enables precise milling with a resolution of up to 0.5 μm, ensuring accurate realization of the intricate slot geometries critical to the SWB HSA performance. However, as with any fabrication processes, small

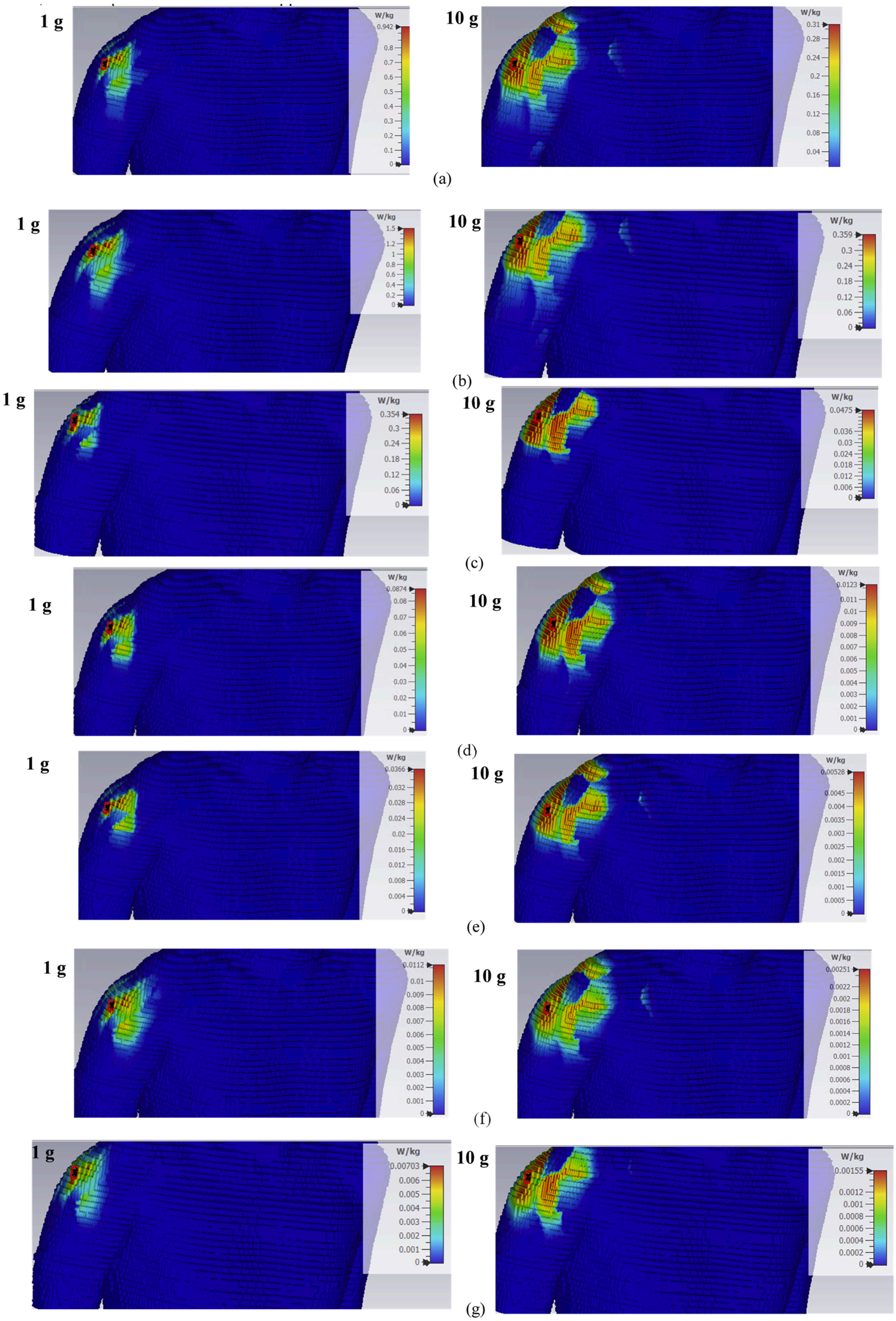

Fig. 13. SAR values for the proposed compact SWB HSA on the arm of the CST-based Gustav phantom body model at (a) 25 GHz, (b) 28 GHz, (c) 38 GHz, (d) 47 GHz, (e) 50 GHz, (f) 57 GHz, and (g) 60 GHz.

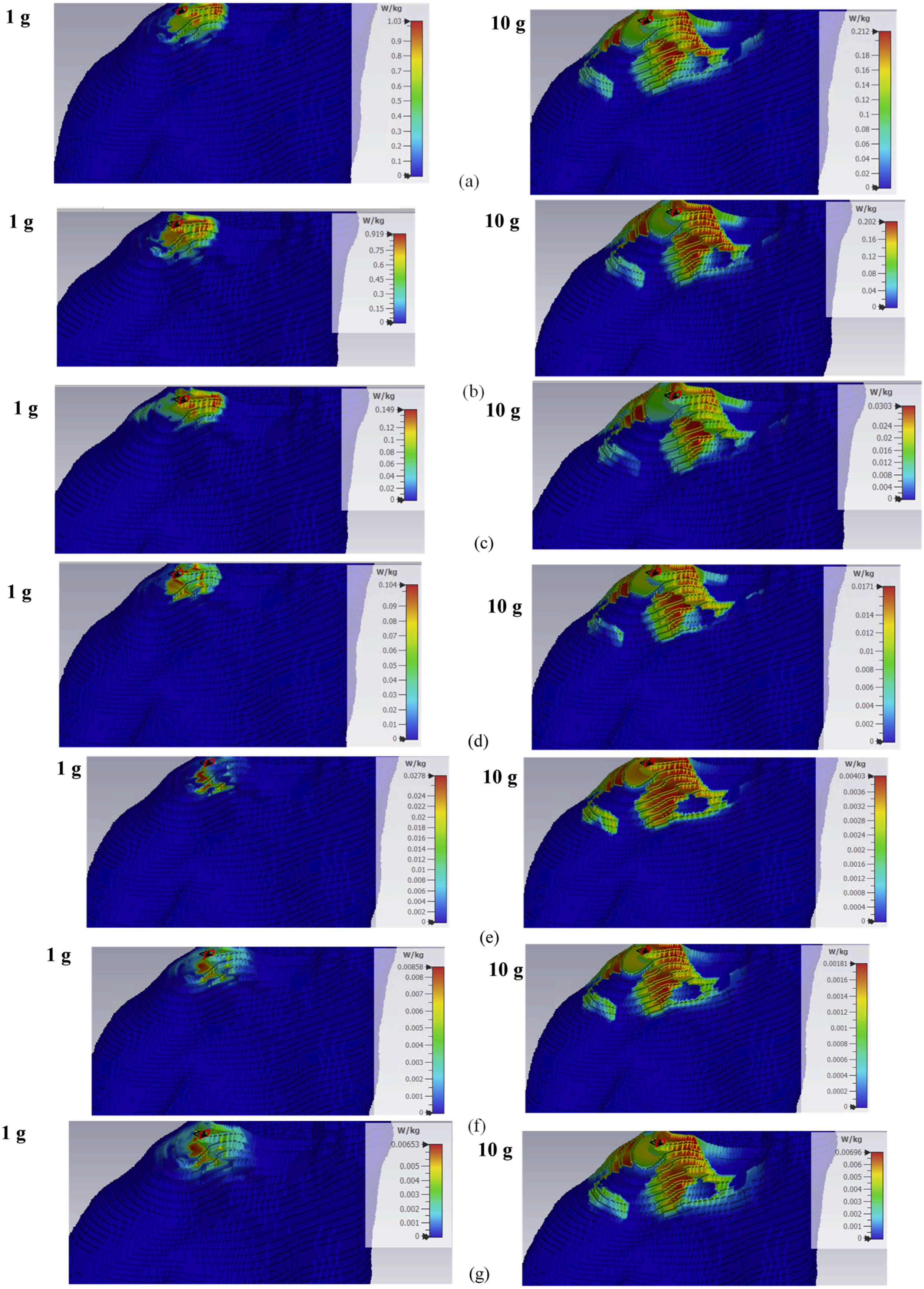

Fig. 14. SAR values for the proposed compact SWB HSA on the shoulder, of the CST-based Gustav phantom body model at (a) 25 GHz, (b) 28 GHz, (c) 38 GHz, (d) 47 GHz, (e) 50 GHz, and (f) 57 GHz, and (g) 60 GHz.

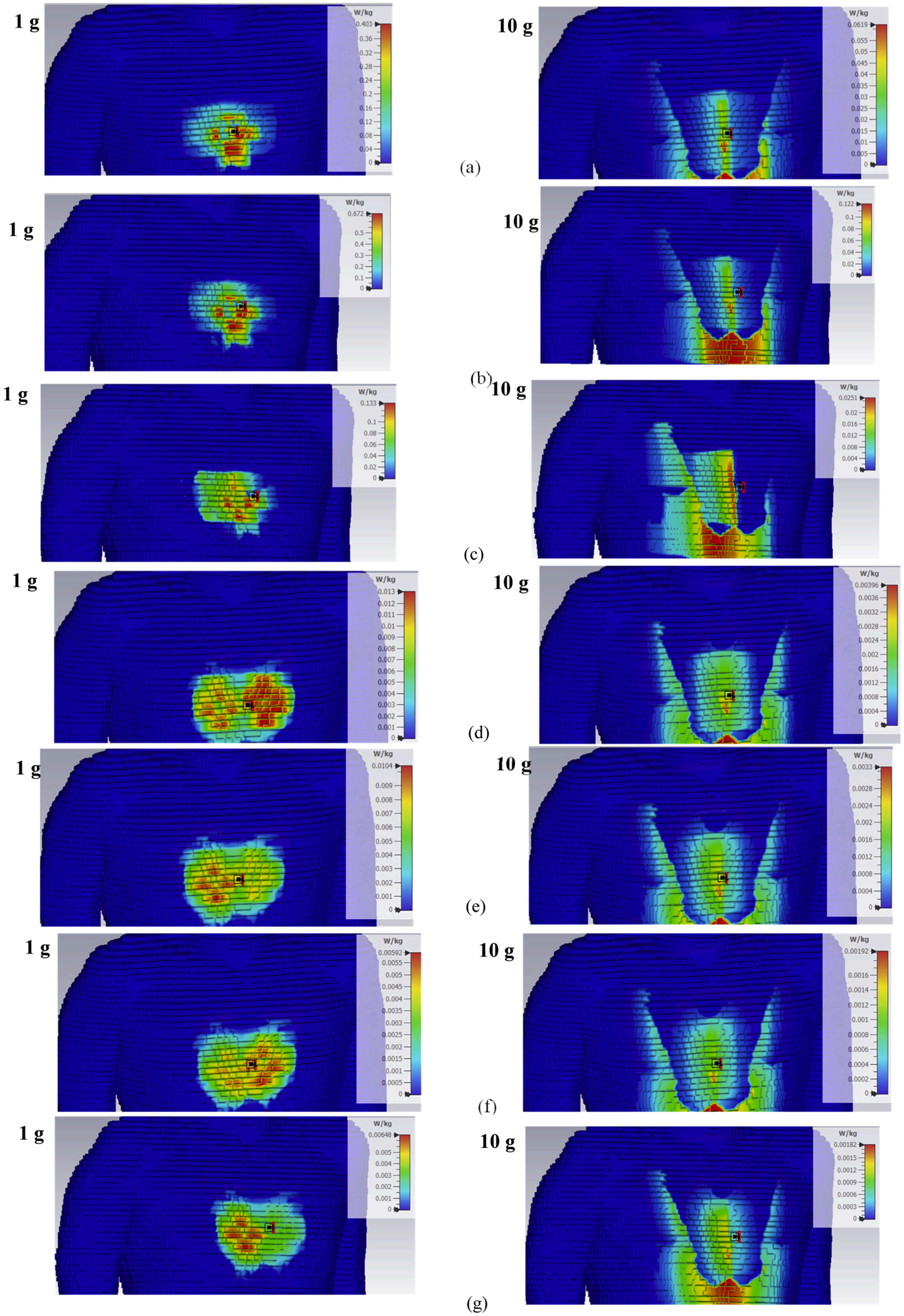

Fig. 15. SAR values for the proposed compact SWB HSA on the chest of the CST-based Gustav phantom body model at (a) 25 GHz, (b) 28 GHz, (c) 38 GHz, (d) 47 GHz, (e) 50 GHz, and (f) 57 GHz, and (g) 60 GHz.

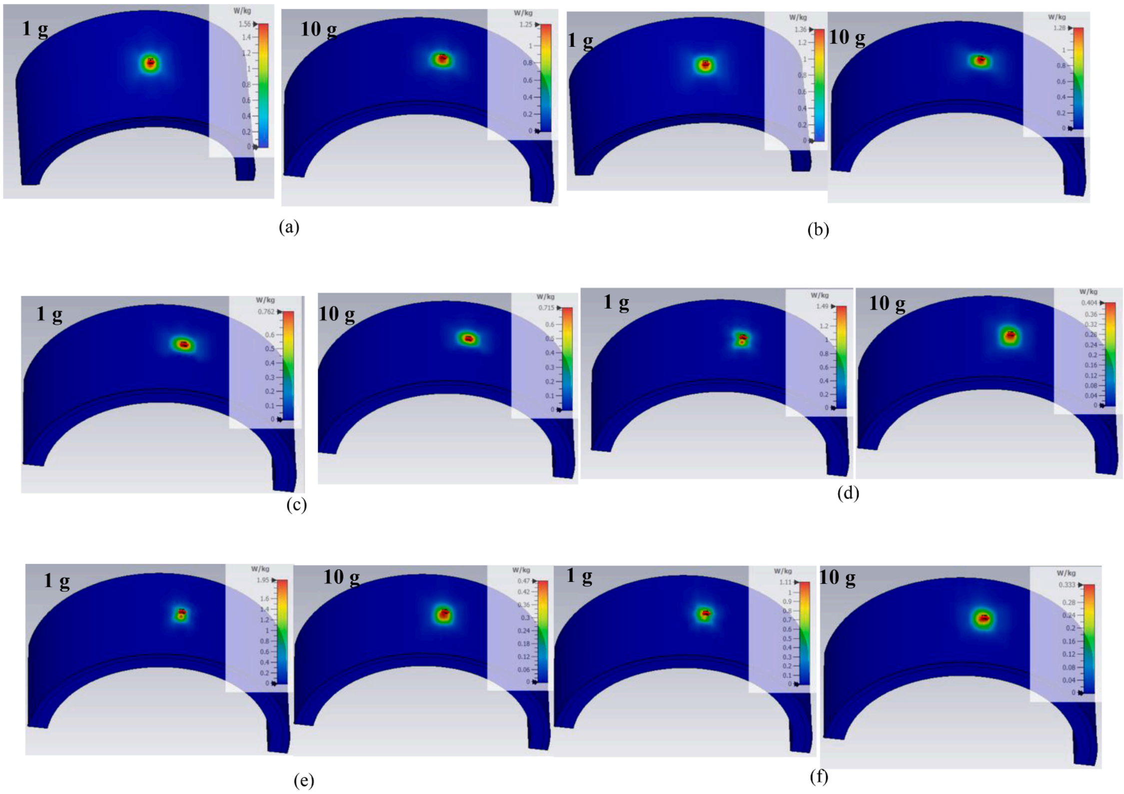

(a) (b) (c) (d) (e) (f)

Fig. 16. SAR values for the proposed compact SWB HSA on the chest of the CST-based cylindrical phantom at (a) 25 GHz, (b) 28 GHz, (c) 38 GHz, (d) 47 GHz, (e) 50 GHz, and (f) 57 GHz.

Table 6
Simulated SAR values for SWB FR2 FR2 on (Gustave CST model and cylindrical phantom).

Freq. (GHz)	Voxel (arm)		Voxel (shoulder)		Voxel (chest)		Cylindrical phantom	
	1 g	10 g	1 g	10 g	1 g	10 g	1 g	10 g
25	0.942	0.310	1.03	0.212	0.403	0.0619	1.56	1.25
28	1.5	0.359	0.919	0.202	0.672	0.122	1.36	1.28
38	0.354	0.0475	0.149	0.0303	0.133	0.0251	0.762	0.712
47	0.0874	0.0123	0.104	0.0171	0.013	0.00396	1.49	0.404
50	0.0366	0.00528	0.0278	0.00403	0.0104	0.0033	1.95	0.47
57	0.0112	0.00251	0.00858	0.00181	0.00592	0.00192	1.11	0.33
60	0.00703	0.00155	0.00653	0.00696	0.00648	0.00182	0.833	0.27

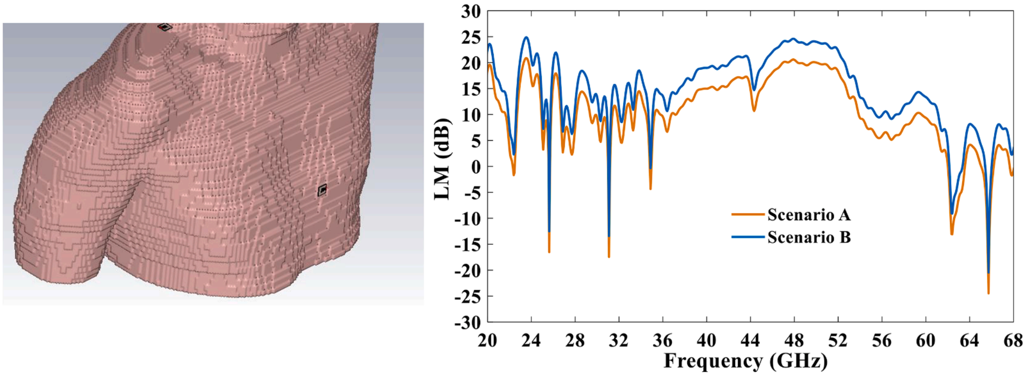

(a) (b)

Fig. 17. (a) Simulated on-body setup showing antennas on the shoulder and chest of a voxel phantom. (b) Link margin versus frequency for two mmWave scenarios: Scenario A & B.

manufacturing tolerances—such as differences in slot width, etching depth, or substrate alignment—can occur. Minor deviations ($\pm$10–20 μm) at mmWave frequencies may affect antenna resonant frequency, impedance matching, and operating BW. To mitigate these impacts, the milling process was carefully calibrated and verified multiple times, and the design incorporates modest tolerance margins to assure strong performance.

The MVG anechoic chamber (10 m × 5 m × 5 m) was used for antenna far field measurement (radiation patterns and gain), which provides a fully isolated environment via absorbers to minimize reflections and external interference during the measurement, which in turn ensures accuracy across the entire required frequency range, making it ideal for wearable antennas. The proposed SWB HSA was fed using a 1.85 mm coaxial connector and connected to one port of a vector network analyzer (VNA), while the chamber's built-in open-ended waveguide probe [47], connected to the other port, was used as the transmitting/receiving element during the scanning process. Basically, near-field measurement is done first, then the measured transmission coefficient (S_{21}) is used for near-field to far-field transformation. It should be noted that to ensure minimal phase and amplitude errors, the probe was carefully aligned, as misalignment at mmWave frequencies can significantly impact pattern fidelity. So in our measurement, we carefully aligned the probes once more before every measurement cycle. To mitigate the cable losses, high-frequency-rated low-loss cables were used, and the calibration stage meticulously de-embedded their effects.

Finally, for gain calibration, a standard gain horn antenna with known characteristics was employed as a reference. The Keysight N5264B performance network analyzer (PNA) was used to measure reflection coefficients (S_{11}). The S_{11} measurement using PNA is shown in Fig. 18(a), while the far-field measurement setup inside the anechoic chamber is shown in Fig. 18(b).

In Fig. 19(a), the reflection coefficient, $S_{11,}$ of SWB HSA highlights its broad impedance matching across the operational mmWave spectrum, which is crucial for achieving reliable communication links in wearable communication environments. Despite its smaller physical size (7.31 mm x 7.31 mm), it maintains competitive matching (Sim.: S_{11} $<$ -11.34 dB over 15.96–<-12.18, 24.66–

62.59=37.93 GHz and Meas.:<-11.86, 24.71– 63.81=39.1 GHz). This resilience, even with size reduction, makes the proposed.

SWB HSA is well-suited for integration in 5 G mmWave wearable applications, where space constraints and efficient power transfer are crucial. In Fig. 19(b), the input impedance profiles for each antenna—illustrated by the real and imaginary components oscillating around 50 Ω and 0 Ω, respectively—further support their strong impedance matching. The stable impedance values across the bandwidth underscore the efficiency of the detailed parametric studies and modifications to the proposed SWB HSA for achieving a balanced and consistent response, even under size constraints. This characteristic contributes to reliable communication, as stable impedance helps avoid impedance mismatch losses that could otherwise disrupt signal integrity, especially in high-data-rate scenarios required for robust communication.

The proposed compact has demonstrated remarkable performance with a high gain, despite its small size. As shown in Fig. 19(c), the gain increases steadily, reaching 3.9 dBi (Sim.) and 3.69 dBi (Meas.) at 34 GHz, and peaking at 7.35 dBi (Sim.) and 7.22 dBi (Meas.) at 56.5 GHz before slightly decreasing at higher frequencies. Fig. 19(c) also illustrates that the measured radiation efficiencies closely match the simulated values, highlighting the design's practical performance. The measured efficiency ranges from 72.45% to 90.88%, compared to the simulated values of 74.38% to 97.17%.

This excellent performance can be attributed to the optimized surface current distribution, as discussed earlier. The concentration of surface currents in critical regions minimizes resistive losses and ensures efficient radiation of input power. This combination of efficient current behavior and compact geometry enables high radiation efficiency, which is particularly important for wearable body-centric applications. The antenna's compact size and firm performance ensure it can operate effectively near the human body, minimizing power loss and maintaining reliable communication within the desired frequency range.

The normalized 2-D polar radiation patterns for the proposed SWB HSA are shown in Fig. 20(a), 20(b), and 20(c) at frequencies of 25 GHz, 40 GHz, and 50 GHz, respectively, for both the E-plane (XY-plane) and H-plane (XZ-plane). The E-plane shows the gain at $\varphi = 0^\circ$ versus elevation angle (θ), and the H-plane shows the gain at $\theta = 90^\circ$ versus azimuth angle(φ). The dashed and dotted curves represent simulated and measured results, respectively. The additional subfigures at $F = 28$ GHz (Fig. 20(a)) illustrate the antenna structure and orientation in the simulation environment, indicating the reference planes used for the radiation pattern extraction. The 2-D patterns correspond to slices of the 3D radiation pattern, where the main lobe orientation aligns with the Z-axis defined in the 3D plot in Table 5. As observed, stable radiation patterns are achieved in both planes, ensuring consistent performance across the super-wideband mmWave frequency range (24.71–63.81 GHz). This stability guarantees reliable signal transmission and reception, which is crucial for body-centric, wearable applications. The ability to maintain good radiation characteristics across varying frequencies further enhances the antenna's suitability for dynamic environments, where signal integrity must be preserved despite variations in size and frequency.

The discrepancy between the simulated and measured results can be attributed to several factors, including fabrication tolerances, variations in measurement setup, and differences in material properties. Minor

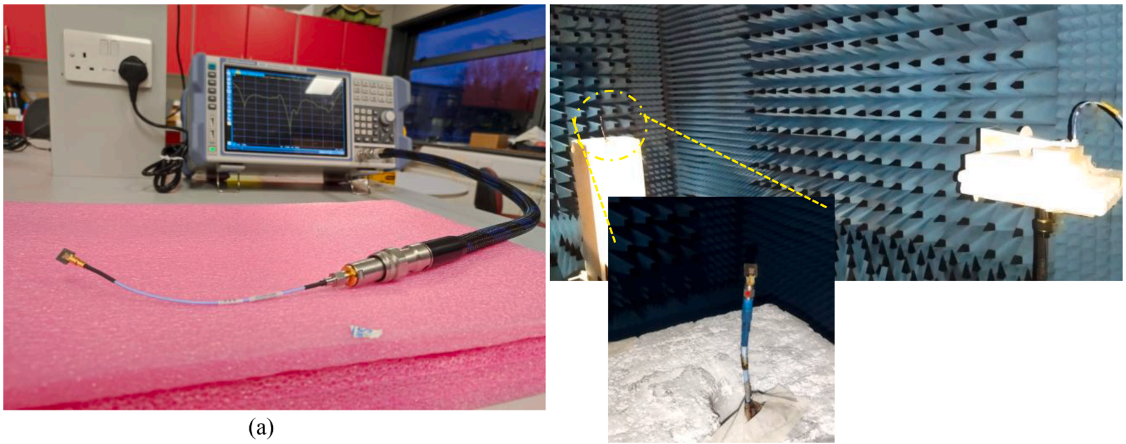
(a)

(b)

Fig. 18. Measurement setup using (a) network analyzer and (b) anechoic chamber.

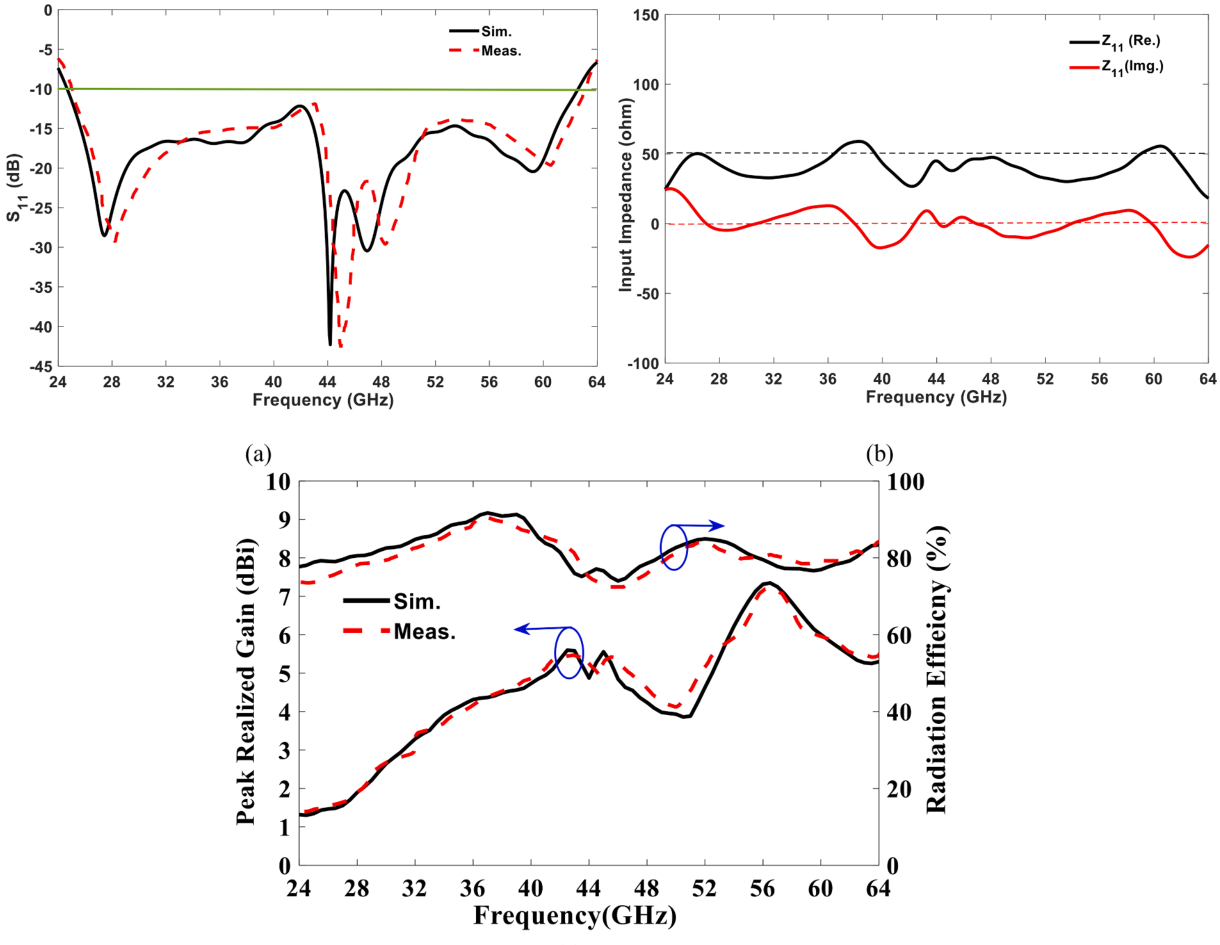

(a)

(b)

(c)

Fig. 19. (a) Simulated and measured S11, (b) Simulated input impedance, and (c) Simulated and measured realized gain with total efficiency of the proposed compact FR2 HSA.

inaccuracies in the manufacturing process, equipment calibration, or antenna positioning during testing can cause deviations. Additionally, the assumption of ideal materials in simulations may not perfectly match real-world conditions. Despite these factors, the overall performance trends, including gain and radiation efficiency, show good agreement, confirming the antenna's practical feasibility for the intended applications.

Finally, Table 7 presents a comparison between the proposed HSA and other recent works in the literature. The proposed antenna stands out as the smallest design while delivering a significantly wider BW and higher gain, making it an excellent candidate for medical wearable applications that demand high data rates and user comfort. Moreover, the proposed antenna has been experimentally tested for flexibility (bending performance) and evaluated for SAR compliance, further confirming its suitability and safety for wearable and body-centric applications. The comparatively higher gain reported in [17,28] is primarily due to their larger dimensions, whereas the compact size of the HSA ensures better integration and enhanced usability in wearable scenarios.

4. Limitations and future work

This study has several limitations despite its promising findings. Although the antenna was successfully tested on the human body (voxel: Sim. and volunteer: Meas.) across different locations, including the chest, shoulder, and arm, the experiments were still conducted under controlled conditions and may not fully capture real-world variability. So, it misses the testing of the antenna performance when it is integrated into a complete wearable system containing a battery, PCB, and fabric. Additionally, the current simulation and experimental validation did not account for environmental and physiological factors, such as human movement, perspiration, and ambient moisture, which in turn will affect HSA performance and signal stability. These factors highlight the need for further validation under realistic, dynamic conditions.

Future work may focus on mitigating these limits by integrating the proposed antenna both in simulation and measurement into a functional wearable system (Battery and fabric) and evaluating their long-term reliability and durability under real-life conditions. Further improvement can be obtained by including additional sensors or electronic components. Moreover, exploring MIMO and diversity configurations using multiple compact HSAs could improve communication robustness, spatial coverage, and resilience to environmental variations. These steps will provide a more comprehensive assessment of the antenna’s capabilities and pave the way for practical deployment in wearable technologies.

5. Conclusion

In this work, a compact super-wide bandwidth Hilbert Slot Antenna (SWB HSA) has been successfully designed, fabricated, and measured for 5 G mmWave applications. The antenna, with a small size of 7.31 × 7.31 mm, provides a super-wide bandwidth of 39.1 GHz, covering the entire Frequency Range 2 (FR2) bands (24.71–63.81 GHz), and achieves a peak gain of 7.22 dBi. Through detailed design evolutions and parametric studies, we have demonstrated that the antenna's

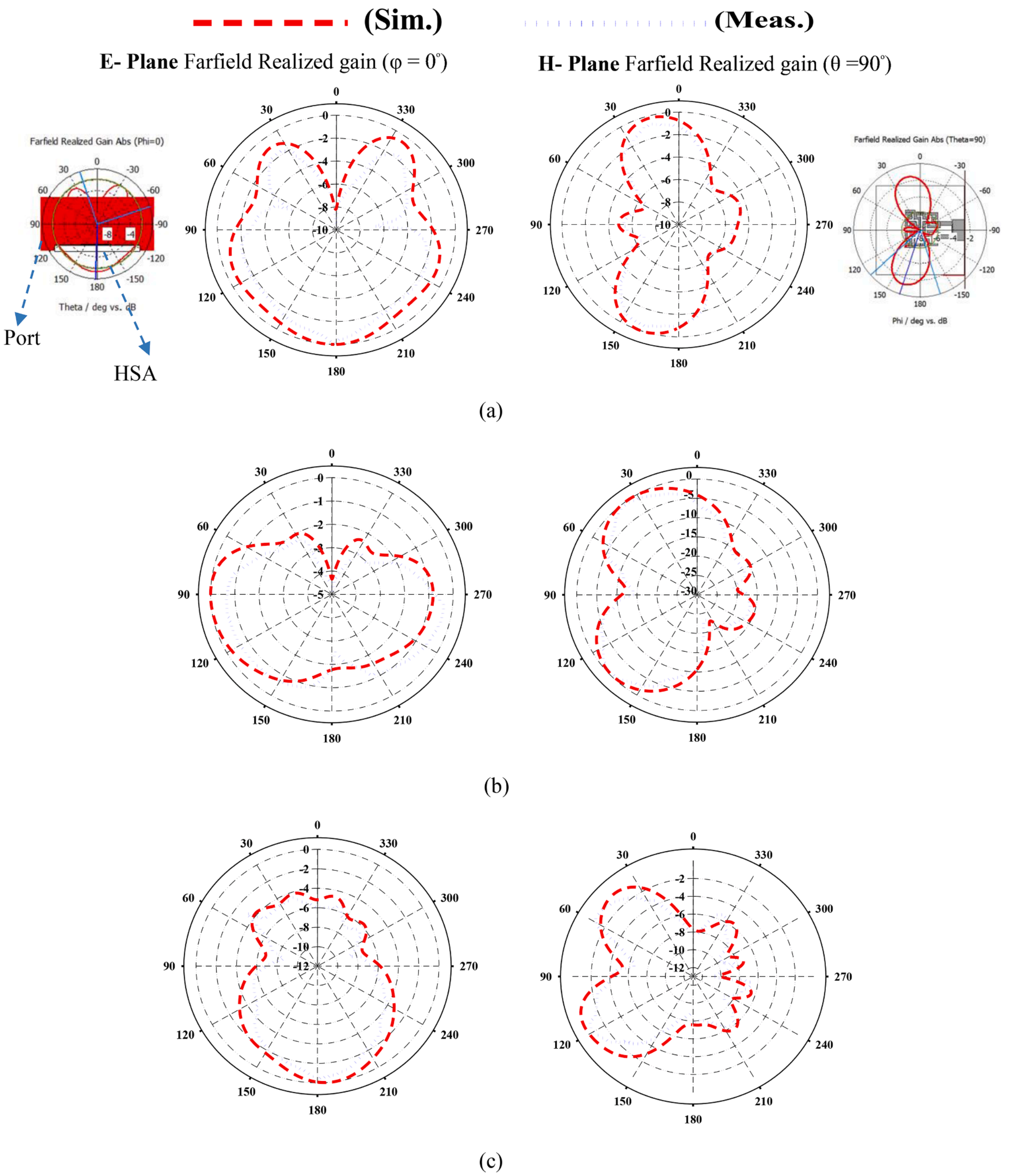

(a)

(b)

(c)

Fig. 20. Simulated and measured radiation pattern of the proposed compact FR2 HAS at (a) $f = 25$ GHz, (b) $f = 40$ GHz, and (c) $f = 50$ GHz.

compact size does not compromise its performance, making it an ideal candidate for high-frequency, space-constrained environments such as wearable and body-centric applications. The antenna's mechanical modifications and its performance in close proximity to the human body have been carefully considered, ensuring that it meets both functional and safety requirements. Moreover, the Specific Absorption Rate (SAR) is found to be within the recommended limits, confirming the antenna's safety for use in wearable devices. Compared to other fractal designs, the proposed HSA achieves super-wideband operation with a simpler geometry and fewer iterations, demonstrating its superior performance and practical feasibility.

Looking ahead, future work will focus on designing a compact Multiple Input Multiple Output (MIMO) antenna system to enhance the reliability and overall performance of the communication system. The integration of MIMO technology will improve signal quality and throughput, making it more suitable for demanding applications in wireless body area networks (WBANs) and other high-performance scenarios. Additionally, replacing the semi-flexible Rogers RT/Duroid 5880 substrate used in this work with a fully flexible or non-fabric substrate could offer improved flexibility and comfort for wearable applications, while maintaining high performance and low loss at mmWave frequencies. These advancements will further contribute to the development of efficient, compact, and reliable antennas for next-generation communication systems.

CRediT authorship contribution statement

Sarmad Nozad Mahmood: Writing – original draft, Validation, Software, Methodology, Investigation, Formal analysis, Data curation, Conceptualization. **Sahar Saleh:** Writing – review & editing, Supervision, Software, Resources, Project administration, Formal analysis, Conceptualization. **Ahmed Nidham Qasim:** Writing – review & editing,

Table 7
Comparison with existing mmWave 5 G wearable antennas in the literature.

Refs.	Substrate	Flexiblity	SAR	Antenna type, (dimension: mm × mm × mm)	BW (GHz)	MG(dBi)	Improvement Methods
[21]	Arlon DiClad 880	No.	No.	Sierpinski Gasket SA (45 × 40 × 0.508)	25–27, 27.5–37.9	6	Parametric studies and controlling the feed position
[13]	Rogers RT/ Duroid 5880	Semi-flexible No bending	No.	Rhombus-inscribed circular ring patch (28 × 17.75 × 1.6) Single(7 × 7.5 × 0.51)	22.8–29.9	10.7 Single: 4.5	1 × 4 corporate feeding network
[16]	cotton	Yes (Sim.)	No.	Arrow-shaped patch, (21.81 × 19.5 × NA)	15.9 –17.2, 22.9 –25.9 & 27.64 – 28.48	4.5	DDEA-SE
[17]	FR4	No.	No.	H-shaped patch, (40 × 40 × 1.6)	27–33	13.2	ANN
[28]	FR4	No.	No.	spherical-shaped patch, (28.2 × 44 × 1.6) single (28.22 × 28.22 × 1.6)	17.7 –28, 8.9–9.9 GHz, 10.4–11.4 13.1–13.7, 15.4–16.2	8.46	DGS
[23]	FR4	No.	No.	Sierpinski Carpet patch, (40 × 40 × 1.6)	29.5–32.6 & 37.5–38.5	5.9	DGS and SIW
[5]	FR4	No.	No.	Sierpinski Carpet patch, (15 × 15 × 1.6)	28.4–38.5, 24.7–25.7, 32.6–36.5 &37.5–38.6	6.1	DGS
[29]	Rogers RT/ Duroid 5880	Semi-flexible No bending	No.	Koch patch, (9 × 9 × 0.508)	26.5–40	5	DGS
Proposed	**Rogers RT/ Duroid 5880**	**Semi-flexible Bending (Sim. & Meas.)**	**Yes**	**HSA, (38.3 × 27.06 × 0.5)**	**24.71– 63.81, 39.1**	**7.22**	**parametric studies**

Software, Resources, Investigation. **Tale Saeidi:** Writing – review & editing, Supervision, Project administration, Funding acquisition, Formal analysis.

Declaration of competing interest

The authors (declare that they have no known competing financial interests or personal relationships that could have appeared to influence the work reported in this paper.

The authors declare the following financial interests/personal relationships which may be considered as potential competing interests:

Data availability

Data will be made available on request.

References

[1] X. Meng, J. Li, D. Zhou, D. Yang, 5G technology requirements and related test environments for evaluation, China Commun. 13 (2016) 42–51.

[2] M.T. Islam, M.T. Islam, M. Samsuzzaman, H. Arshad, H. Rmili, Metamaterial loaded nine high gain Vivaldi Antennas array for microwave breast imaging application, IEEE Access 8 (2020) 227678, https://doi.org/10.1109/ACCESS.2020.3045458.

[3] S. Saleh, T. Saeidi, N. Timmons, F. Razzaz, A comprehensive review of recent methods for compactness and performance enhancement in 5G and 6G wearable antennas, Alex. Eng. J. 95 (2024) 132–163, https://doi.org/10.1016/J.AEJ.2024.03.097.

[4] T. Saeidi, S.N. Mahmood, S. Saleh, N. Timmons, A.J.A. Al-Gburi, F. Razzaz, Ultra-wideband (uwb) antennas for breast cancer detection with microwave imaging: a review, Results Eng. 25 (2025) 104–167.

[5] A. Raj, D. Mandal, Design and performance analysis of fractal slot array antenna for advanced 5G mm-wave applications, Int. J. Electr. 112 (2025) 1821, https://doi.org/10.1080/00207217.2024.2408788.

[6] U.R. Khan, J.A. Sheikh, A. Junaid, R. Amin, S. Ashraf, S. Ahmed, Design of a compact hybrid Moore's fractal inspired wearable antenna for IoT enabled bio-telemetry in diagnostic health monitoring system, IEEE Access 10 (2022) 116129–116140.

[7] S. Hassan Ghadeer, S. Kamal Abd.Rahim, M. Alibakhshikenari, B.S. Virdee, T. A. Elwi, A. Iqbal, M. AlHasan, An innovative fractal monopole MIMO antenna for modern 5G applications, AEU - Int. J. Electr. Commun. 159 (2023) 154480, https://doi.org/10.1016/j.aeue.2022.154480.

[8] Y. Jiang, S. Yang, X. Shen, J. He, H. Tang, A high gain conformal antenna based on Hilbert fractal for capsule endoscopy application, in: Proceedings of the ICMMT - International Conference on Microwave and Millimeter Wave Technology, 2024. Institute of Electrical and Electronics Engineers Inc.

[9] K. Cao, Y. Xu, W. Li, J. Wang, W. Lu, Z. Li, A design of miniaturized ultra-shortwave fourth order Hilbert fractal rectifier antenna, IEICE Electr. Express 21 (2024) 20240032, https://doi.org/10.1587/elex.21.20240032.

[10] P. Mohanty, S. Pandav, S.K. Behera, Circularly polarized hybrid fractal antenna for Ku band application, AEU - Int. J. Electr. Commun. 190 (2025) 155641, https://doi.org/10.1016/j.aeue.2024.155641.

[11] S. Saleh, T. Saeidi, N. Timmons, C. McDaid, S. Karamzadeh, Semi-flexible compact wi-fi 6E Hilbert curved based antenna for wearable applications, in: Proceedings of the 6th International Conference on Bio-Engineering for Smart Technologies (BioSMART), 2025.

[12] W. Li, W. He, Z. Lai, S. Liu, Study of A 28-GHz tree-shaped fractal millimeter wave antenna, in: Proceedings of the IOP Conference Series: Earth and Environmental Science 558,, 2020, p. 052,026. IOP Publishing Ltd.

[13] M.U. Tahir, U. Rafique, M.M. Ahmed, Rhombus-inscribed circular ring fractal array antenna for millimeter-wave 5G applications, Int. J. Antennas Propag. 2022 (2022) 1, https://doi.org/10.1155/2022/8254785, 2022.

[14] Y. Feng, Z. Wang, D. Shen, H. Yuan, D. Hou, S. Lin, Q. Chen, An ISGW-based 5G millimeter wave ultra-bandwidth, high-gain fractal magnetic dipole antenna, in: Proceedings of the IEEE MTT-S International Microwave Workshop Series on Advanced Materials and Processes for RF and THz Applications, IMWS-AMP 2022 - Proceedings, 2022. Institute of Electrical and Electronics Engineers Inc.

[15] S.M. Rizvi Jarchavi, N. Hussain, M. Soruri, M. Alibakhshikenari, F. Arpanaei, C. Stefanovic, B.S. Virdee, A high-gain quasi-fractal antenna with wide range operation for 5G applications over V-band spectrum, in: Proceedings of the IEEE-APS Topical Conference on Antennas and Propagation in Wireless Communications, APWC 2022, 2022, pp. 99–102. Institute of Electrical and Electronics Engineers Inc.

[16] N.K. Mallat, A. Jafarieh, H. Noorollahi, M. Nouri, A novel fractal arrow-shaped mmWave flexible antenna for IoT and 5G communication systems, Prog. Electromagn. Res. Lett. 107 (2022) 9–17.

[17] R. Karanam, D. Kakkar, Artificial neural network optimized ultra wide band fractal antenna for vehicular communication applications, Trans. Emerg. Telecommun. Technol. 33 (2022), https://doi.org/10.1002/ett.4620.

[18] S. Enahoro, S.C. Ekpo, M. Uko, S. Alabi, F. Elas, R. Unnikrishnan, A Metamaterial-Grounded Ultra-Wideband Cross-Fractal MIMO Antenna for K, Ka, and Mmwave Applications, Ka, and Mmwave Applications, 2024.

[19] H. Imane, B. Mohammed, B.R. Ilyas, Antenna design based on fractal geometry compact for several application on 33Ghz and 35 ghz, Przeglad Elektrotech. 1 (2024) 249, https://doi.org/10.15199/48.2024.09.48.

[20] K. Shet, G.S. Karthikeya, H.S. Suraj, A wideband probe-fed low cost mm wave fractal antenna array for 5G, in: Proceedings of the Journal of Physics: Conference Series 1,706,, 2020, p. 012,094. IOP Publishing Ltd.

[21] V. Harini, M.V.S. Sairam, R. Madhu, Performance analysis of an extended Sierpinski Gasket fractal antenna for millimeter-wave femtocells applications, Wirel. Pers. Commun. 119 (2021) 1437–1468, https://doi.org/10.1007/s11277-021-08289-3.

[22] M.M. Jawad, N.N.N.A. Malik, N.A. Murad, M.R. Ahmad, M.R.M. Esa, Y.M. Hussein, Design of substrate integrated waveguide with minkowski-sierpinski fractal antenna for wban applications, Bull. Electr. Eng. Inform. 9 (2020) 2455–2461, https://doi.org/10.11591/eei.v9i6.2194.

[23] A. Raj, D. Mandal, Design and analysis of Sierpinski fractal antennas for millimeter-wave 5G and ground-based radio navigation applications, Trans. Emerg. Telecommun. Technol. 35 (2024), https://doi.org/10.1002/ett.70001.

[24] P. Garu, W.C. Wang, Design and analysis of a PDLC-based reconfigurable Hilbert fractal antenna for large and fine THz frequency tuning, Micromachines 13 (2022) 964, https://doi.org/10.3390/mi13060964 (Basel).

[25] A. Mondir, M.A. Ennasar, L. Setti, F. Mustapha, Design, analysis, of high performance antennas for 5G communications analysis using WCIP, Prog. Electromagn. Res. C 135 (2023) 211.

[26] A.K. Sidhu, J.S. Sivia, Design of wideband fractal MIMO antenna using Minkowski and Koch hybrid curves on half octagonal radiating patch with high isolation and gain for 5G applications, Adv. Electromagn. 12 (2023) 58–69.

[27] A. Raj, D. Mandal, Comparative analysis of the 2X2 patch antenna array with modified fractal antenna for 5G communication and wireless applications, in: Proceedings of the IEEE Microwaves, Antennas, and Propagation Conference, MAPCON 2022, 2022, pp. 670–675. Institute of Electrical and Electronics Engineers Inc.

[28] N. Bisht, P.K. Malik, S. Das, T. Islam, S. Asha, M. Alathbah, Design of a modified MIMO antenna based on tweaked spherical fractal geometry for 5G new radio (NR) band N258 (24.25–27.25 GHz) applications, Fractal Fract. 7 (2023) 718, https://doi.org/10.3390/fractalfract7100718.

[29] R. Kassym, T. Balgynbek, T. Serikov, P. Ahmetova, G. Sergazin, K. Ozhikenov, T. Sultangaziyev, P. Kumar, A. Tlenshiyeva, N. Yernazarov, Development a novel design of miniaturized Heptagonal Koch fractal wide band Antenna for 5g mm wave and IoT applications, East.-Eur. J. Enterpr. Technol. 3 (2024) 6–14, https://doi.org/10.15587/1729-4061.2024.306712.

[30] S.I. Orakwue, M.I. Ehikhamenle, Design of a Tri-band Minkowski fractal MIMO antenna for FR2 5G applications, J. Eng. Res. Rep. 26 (2024) 190–205, https://doi.org/10.9734/jerr/2024/v26i91272.

[31] J. Zhu, A. Hoorfar, N. Engheta, Bandwidth, cross-polarization, and feed-point characteristics of matched Hilbert antennas, IEEE Antennas Wirel. Propag. Lett. 2 (2003) 2–5.

[32] H. Imane, B.I. Ridha, H. Yassine, B. Riyadh, Study and simulation of Sierpinsky Carpet fractal antenna for millimeter waves, in: Proceedings of the 2nd International Conference on Electrical Engineering and Automatic Control, ICEEAC 2024, 2024. Institute of Electrical and Electronics Engineers Inc.

[33] H. Sagan, Space-Filling Curves, Springer Science & Business Media, 2012.

[34] M. Bader, Space-Filling Curves: An Introduction With Applications in Scientific Computing, Springer Science & Business Media, 2012.

[35] Anon, 2026 em: talk - microstrip patch antenna calculator, https://www.emtalk.com/mpacalc.php?er=2.2&h=0.508&h_units_list=hmm&fr=42.5&Operation=Synthesize&La=&L_units_list=Lmm&Wa=&W_units_list=Wmm&Rin=.

[36] D.S. Wadhwa, P.K. Malik, J.S. Khinda, Improvement in 5 dBi gain-bandwidth of wide band antenna for indoor K–, Ka –Band, millimeter-wave applications, J. Infrared. Millim. Terahertz. Waves 43 (2022) 527–549, https://doi.org/10.1007/s10762-022-00865-3.

[37] H. Liu, Z. Yang, Y. Gao, L. Dong, Y. Guo, X. Xu, T. Meng, W. Hu, C. Feng, High-frequency gain enhancement of a broadband metasurface antenna with parasitic patches using characteristic mode analysis, Front. Phys. 13 (2025), https://doi.org/10.3389/fphy.2025.1638385.

[38] S. Saleh, T. Saeidi, N. Timmons, B. Alali, F. Razzaz, A.A. Althuwayb, High-performance UWB Vivaldi antenna on FR4: a cost-effective solution for wearable technologies, Results Eng. 25 (2025) 104230, https://doi.org/10.1016/j.rineng.2025.104230.

[39] A.S. Burra, B. Roy, Design and evaluation of a compact unified hexagonal dual-band wearable patch antenna, Heliyon 11 (2025) e42868, https://doi.org/10.1016/j.heliyon.2025.e42868.

[40] A.S. Burra, B. Roy, Design and development of a truncated patch antenna with slot loading for wearable devices, in: Proceedings of the IEEE Microwaves, Antennas, and Propagation Conference, MAPCON 2024, 2024. Institute of Electrical and Electronics Engineers Inc.

[41] S. Saleh, T. Saeidi, N. Timmons, B. Alali, F. Razzaz, A.A. Althuwayb, Compact ultra-wide band two element vivaldi non-uniform slot MIMO antenna for body-centric applications, Results Eng. 24 (2024) 102839, https://doi.org/10.1016/j.rineng.2024.102839.

[42] T. Saeidi, S. Saleh, N. Timmons, S. Karamzadeh, A.J.A. Al-Gburi, F. Razzaz, Enhancing connectivity/mobility in WBAN applications through detachable wearable multi-band MIMO antenna, Phys. Scr. 99 (2024) 075315, https://doi.org/10.1088/1402-4896/ad5887.

[43] Standards Committee of the IEEE Computer Society, M., IEEE Std 802.15.6-2012, IEEE Standard for Local and Metropolitan Area Networks–Part 15.6, Wireless Body Area Networks, 2012.

[44] 5G; Study on channel model for frequencies from 0.5 to 100 GHz (3GPP TR 38.901 version 16.1.0 Release 16). (2020).

[45] Hussain Abbasi, Q.: Radio channel characterisation and system-level modelling for ultra wideband body-centric wireless communications. (2012).

[46] ProtoMat S104 - RF and Microwave PCB Prototyping | LPKF, access Feb. 2026.

[47] Open-Ended Waveguides: Measurement probes and feeds, 2026 https://www.mvg-world.com/en/products/antennas/measurement-probes-and-feeds/open-ended-waveguides.